A multi-disciplinary characterization and forecast of a unique fog event: microphysics measurements, mesoscale modeling and machine learning

By Anton Gelman[1*], Ayala Ronen[2], Pavel Kunin[3], Tamir Tzadok[1], Eyal Agassi[1], Rong-Shyang Sheu[4], Adam Pietrkowski[5], Dorita Rostkier-Edelstein[1,2] .

1 The Fredy and Nadine Institute of Earth Sciences, The Hebrew University of Jerusalem, Jerusalem, Israel

2 Department of Environmental Physics, Israel Institute for Biological Research, Ness Zyiona, Israel

3 Life Science Research Institute, Ness Zyiona, Israel

4 Research Applications Laboratory, National Center for Atmospheric Research, Boulder, CO, United States

5 Forecasting Center, Tel-Aviv, Israel

* Corresponding author

Submitted to Journal of Geophysical Research

2023

Key points:

WRF-RTFDDA mesoscale forecasts, processed thresholds and ML algorithms, succeeded in predicting the development of the fog.

WRF-RTFDDA forecasts distinguish near-surface fog and elevated fog/low clouds, which is not possible from satellite imagery only.

Clear patches of fog at coastal areas covered in part by urban landuse were observed both in satellite imagery and model forecasts.

Abstract

We present a multidisciplinary study of the microphysics, mesoscale and synoptic conditions of a rare radiation-fog event in the central and southern regions of Israel during January 3-6, 2021. The fog developed during nighttime from south to central coastal areas and dissipated at morning. The synoptic conditions were dominated by Red Sea Troughs at the surface without cyclonic upper air circulation, suitable for radiation fog development. In-situ measurements were combined with satellite imagery, high resolution (1-km grid size) Weather Research and Forecast model (WRF) with Real-Time Four-Dimensional Data Assimilation (RTFDDA) forecasts and post-processing algorithms including machine learning (ML) to analyze this event and to evaluate its numerical forecasting. The micro-physical analysis involved measurements of droplet size distribution and visibility range, allowing the calculation of liquid-water content and effective diameter of fog droplets. The measured visibility range was 90 m. The droplet diameter main mode was 1-2 micrometers, followed by another one around 6 micrometers. Typical liquid-water content values were 0.01-0.025 g/m^3. WRF-RTFDDA mesoscale forecasts, post-processed by simple thresholds-based and ML algorithms, largely succeeded in predicting the temporal and spatial development of the dense fog. They proved useful in distinguishing between near-surface fog and elevated fog/low clouds, a distinction not possible from satellite imagery only. Clear patches at coastal areas covered in part by urban landuse were observed both in satellite imagery and model forecasts. WRF-RTFDDA forecasts proved their usefulness in forecasting this massive fog and low clouds events and in providing alerts to operational users and field campaign deployments.

Keywords: fog, WRF, forecast, data assimilation, machine learning, microphysics

Plain Language Summary

We studied a rare and thick fog that happened in Israel in January 2021. The fog appeared at night and disappeared in the morning. It covered a large area from the south to the center of the country. The fog was caused by warm and moist air coming from the Red Sea. We used different methods to measure and understand the fog, such as satellites, weather models, and instruments on the ground. We found that the fog had very small water droplets, about 1-6 micrometers in size, and a low amount of water in them. These made the fog hard to see through and hard to predict. We also found that the fog was affected by the cities along the coast, which created some clear spots in some places. Our weather models were able to forecast the fog well and to tell the difference between fog near the ground and clouds higher up. Our study helps to learn more about how fog forms and behaves in this region and how to improve its forecasting.

1. Introduction

Fog is a specific meteorological condition, that reduces the visibility at the Earth's surface, which distresses many human activities, such as aviation and ground transport. As a spatial bulk phenomenon, it depends on the geographical region, terrain properties, synoptic and mesoscale conditions and time of day, among the most significant factors.

It is complicated to determine the exact appearance parameters of a fog event, since fog occurrence, development, and dissipation is determined by the multiple simultaneous processes (microphysical, radiative, dynamical, thermodynamical), with a wide range of conditions, that interact nonlinearly (Haeffelin et al., 2010). Thus, most of the many fog measurements reported in the scientific literature characterizing fog worldwide are on the local scale.

In Israel, fog generally appears after midnight and exists until approximately four hours after the sunrise, in some extreme cases it persists for more than 10 hours. (Levi, 1967) thoroughly described fog in Israel, including its typical synoptic conditions, and identifies radiative and advection as the most common mechanisms of its development in Israel.

During the four consecutive nights and mornings of 3-6 January 2021 fog developed over the central and southern regions of Israel reducing visibility to an unprecedented extent. The special report issued by the Israel Meteorological Service (IMS (https://tinyurl.com/mv3jbtkt, in Hebrew, accessed on 28 April, 2021) states that this meteorological phenomenon was unusual for the winter months; this radiation fog event was triggered by the dry weather, which is unseasonable for Israel's winter

Radiation fog forms when the weather is relatively stable, with cold ground temperatures and low wind speeds. A dry layer above the sea breeze and air pollution can also contribute to the formation of heavy fog. The polluted air traps water droplets effectively and intensify the fog. This type of fog is common on long winter nights when the radiative cooling of the marine layer is prevented by humidity.

(Alpert et al., 2004) developed an automatic semi-objective classification of synoptic patterns in the eastern Mediterranean, which allows classifying the January fog event as a Red Sea Through (RST) with eastern axis on January 3rd, and RST with western axis on January 4th-6th. RST is one of the 5 main radiation fog conditions that are possible in Israel as described by (Levi, 1967). The RST, or Red Sea Trough, is an extension of the Sudan low that lies within the intertropical convergence zone. The counterclockwise flow of winds from the east or south-east direction dries the air. RST are mostly frequent during the fall and spring seasons but develop with lower probability during summer and winter, too (Goldreich, 2003).

During the January 3-6, 2021, fog event we performed a comprehensive field campaign that included several ground-based monitoring instruments, both in-situ and remote sensing. The remote sensing setup included a thermal IR Whole Sky Imager and a Doppler lidar. These measurements showed that radiation fog development is characterized by three distinctive properties: azimuthal symmetrical shape during the buildup phase, zenith brightness temperature and ground level air temperature have very close values, and sharp rise from very little cloud cover, to completely overcast sky ((Ronen et al., 2021).

The aim of the current study is to analyze further aspects of the January 3-6, 2021 fog event: the synoptic, mesoscale and micro-physics characteristics. We analyzed the synoptic conditions responsible for the studied event using the reanalysis data from the National Center for Environmental Prediction/National Center for Atmospheric Research Reanalysis Project (defined hereafter as NNRP, described by (Kalnay et al., 2001; Kistler et al., 2001)). The mesoscale features were characterized with the help of EUMETSAT fog observations and short range WRF-RTFDDA forecasts operationally issued during the event. The micro-physics analysis will include mainly the characteristic droplets size distribution, the effective radius and the Liquid Water content (LWC).

We analyze the ability of forecasting the event with the high resolution (1-km grid size) Weather Research and Forecast model [WRF, (Skamarock et al., 2021)] with Real-Time Four-Dimensional Data Assimilation [RTFDDA, (Huang et al., 2018)] system post-processed by a simple thresholds and machine learning (ML) algorithms.

The scientific measurements and analysis presented in the present manuscript and in Ronen et al. (2021) publications comprise a unique and most comprehensive description of a fog event in Israel and provide significant insight into its formation and its characterization.

2. Methods and data

The methods presented in this section can be classified into two parts: actual physical measurements and numerical weather predictions (NWP) models. The physical measurements are either in situ (surface and upper air) or spaceborne remote sensing. Two meteorological and synoptic models were used. Each method provides unique insight into the fog event, and the synergy between all of them allows us a comprehensive description of it.

2.1. Observations

2.1.1 In situ

Our field campaign was held during January 3-6, 2021 at the Israel Institute for Biological Research in Ness Ziona, located about 8 km east of the Mediterranean Sea over flat terrain (see Fig.1a). In-situ observations of the fog droplets size distribution and the visibility range were performed in an open area on a small hill with height of 40 m above sea level. The droplet size distribution was measured by the optical Forward Scattering Spectrometer Probe FSSP-100 [PMS, USA], shown in Fig.1b. It was set to measure droplet sizes up to 16 microns with temporal resolution of 1 sec. The spectrometer was pre-calibrated with a Flow Focusing Monodisperse Aerosol Generator 1520 [TSI, USA]. A SWS250 [Biral, GB], presented in Fig.1c and performed continuous measurements of the visibility range. Temperature and humidity data were obtained from close meteorological stations “Rehovot” (Israel Ministry of Agriculture, https://meteo.moag.gov.il/home/map?TargetIds=11) and “Bet Dagan” [Israel Meteorological Service (IMS), https://ims.data.gov.il). IMS radiosondes data were available from “Bet-Dagan” station, too. The vertical profiles of temperature, horizontal winds, relative humidity, mixing ratio and dew point temperature were used in this study. The three aforementioned stations are located less than 10 km from the field campaign location and have the same climatological characteristics (see Fig. 1a).

[Figure 1]

2.1.2. EUMETSAT imagery

The EUMETSAT satellites family is a group of geostationary satellites that carry the Spinning Enhanced Visible and InfraRed Imager (SEVIRI) instrument (https://www.eumetsat.int/seviri).

SEVIRI is a multispectral imager that can provide the Earth's observations in 12 spectral channels, providing more precise data throughout the atmosphere than previous systems. SEVIRI can measure the temperatures of the land surface, clouds, sea surface, as well as the distribution of different gases such as water vapor, ozone and CO_2 in the air. SEVIRI data are used for various applications, such as NWP, climate monitoring, sea surface temperature analysis and detection of severe weather events. SEVIRI is the primary instrument on the Meteosat Second Generation (MSG) satellites, which are operated by EUMETSAT, the European Organisation for the Exploitation of Meteorological Satellites.

The images for night times composed of data from a combination of the SEVIRI IR3.9, IR10.8 and IR12.0 channels, developed by EUMETSAT (https://navigator.eumetsat.int/product/EO:EUM:DAT:MSG:FOG, March 2022), for January 3-6, 2021, at night times were used. As reported by EUMETSAT (https://www-cdn.eumetsat.int/files/2020-04/pdf_rgb_quick_guide_night_micro.pdf, March 2022) this so RGB product provides the best color contrast between fog/low cloud and cloud-free area at night. However, fog and low clouds are not separable from each other based only on their colors. The thinner the low clouds/fog the more the color looks like that of the ground (pinkish). The detection of very thin fog/low clouds is problematic. The images used for day times during the studied period come from the Natural Color RGB product. The product uses three solar channels: NIR1.6, VIS0.8 and VIS0.6. The small droplets of water clouds have large reflectance at all channels and therefore appear whitish. However, it should be noted that the droplets-size identification here is semi-quantitative as opposed to the in-situ observations in our measurements campaign described in sections 2.1 and 2.2.

Here we objectively estimated satellite-derived foggy areas by using "night_fog" composite for night fog and 'fog' composite for day fog, which are available in SatPy library, described by (Raspaud et al., 2021). The "night_fog" composite uses 3 channels: IR039, IR108 and IR120. It produces differences between channels, and fog might be assigned to areas where differences between IR120 and IR108, IR108 and IR039 fall in ranges -4 K to 2 K and 0 K to 10 K, respectively. The values of the IR108 channel should be within 263 K to 293 K (Eronn, 2007; Erturk and Prieto, 2010). The 'fog' composite also needs 3 channels, but instead of IR039 the channel IR087 is used, the difference between IR108 and IR087 should fall in the range 2 to 6 K.

2.2 Models and calculations

2.2.1 Synoptic analysis

We analyzed the synoptic flow during the period of January 3-6, 2021, using the NNRP

reanalysis. This database is available as daily means or as single values every 6 hours from 1948-present on a 2.5° X 2.5° grid spacing. The NNRP reanalysis has been extensively used to characterize the synoptic flow in the eastern Mediterranean, including the semi-objective classification of synoptic weather regimes since 1948 (Alpert et al., 2004) and recently for the development of an automatic identification algorithm of Red Sea Troughs (Saaroni et al., 2020).

2.2.2 WRF-RTFDDA mesoscale forecasts

The WRF model is a highly advanced mesoscale NWP model that serves both operational forecasting and atmospheric research needs. It includes prognostic variables such as horizontal and vertical wind components, microphysical quantities, potential temperature, geopotential, and surface pressure. The model has a nesting capability that allows including high-resolution grids in geographic domains within coarser grids. The WRF model also includes a wide range of physical formulations to simulate atmospheric and land-surface physics. For more information on the WRF modeling system, please refer to, e.g., (Skamarock et al., 2021).

The operational forecasts used in the work employ the WRF model (version 3.7) with the Advanced Research (ARW) WRF solver for the simulations. The forecasts were run with a nested domains configuration of 9, 3 and 1 km horizontal resolution (Fig.2a-c) and 57 vertical levels. The land use of the most inner domain can be seen in Fig. 2d.

[Figure 2]

The WRF physical schemes used are shown in in the Supporting Materials, Table 1.

Developed at NCAR/RAL, RTFDDA is a WRF-based real-time four-dimensional data assimilation and short-term forecasting system that efficiently assimilates a wide range of observations for real-time NWP (Huang et al., 2018). WRF-RTFDDA relies on Newtonian-relaxation based data assimilation to create mesoscale analysis or reanalysis that combine observations and model dynamics. The assimilation of observations using RTFDDA has been proven to improve the mesoscale flow [(Liu et al., 2008) and references therein]. Analysis and forecasts from the Integrated Forecast System [IFS, (Owens and Hewson, 2018)] developed by the European Centre for Medium-Range Weather Forecasts (ECMWF) were used for initial and boundary conditions. Operational forecasts at 1000 and 975 hPa vertical levels were made available for this study to identify fog areas.

2.2.3. Thresholds Algorithm (TA) for WRF-RTFDDA fog-conditions identification

Simulation of radiation fog development is one the most difficult challenges in NWP, among others due to the limitations of the models in simulating stable conditions and the coarse microphysical parameterizations. Therefore, it is common practice to forecast fog as a diagnostic variable, based on forecast conditions of relative humidity, temperature and wind

speed. The thresholds algorithm (TA) that we applied in order to identify the fog events in the model forecasts was based on a combination of three thresholds: a 2-m relative humidity (RH) threshold of more than 90%, 10-m wind speed (WS) threshold of 2-m/s or less, and dew point depression (difference between 2-m temperature and 2 m dew point temperature, $T-T_d$) threshold of 2.2 of less. Similar options were chosen in (Nilo et al., 2020).

2.2.4. Algorithm for machine-learning fog-identification from model forecasts

2.2.4.1. A review of machine-learning fog-identification algorithms

ML is a powerful technique, which allows revealing implicit dependencies and regularities. ML works both with ordered and disordered data, but a different approach is needed in these two cases. For example, a neural network is a better fit for disordered data, than a random forest algorithm, but random forest is more suitable for ordered data without gaps.

Many have been undertaken to investigate satellite-derived fog and other parameters by using ML methods, such as gradient boosted trees (Kim et al., 2020), random forest and a few others, including neural networks approach, which may be found in (Papin et al., 2002). Techniques used by these authors were similar and based on comparison of satellite imagery results with results of ground measurements or modeling. Satellite results were interpreted as labels and ground measurements were interpreted as features. Then the appropriate model was chosen, and its prediction results were compared with a verification set of satellite data. Aforementioned authors demonstrated good fit between their models and measured data. A similar approach was used here to identify patterns in model data similar to the EUMETSAT fog patterns.

2.2.4.2. Machine-learning algorithm for WRF-RTFDDA fog-conditions identification

Here we investigated the possibility of applying ML methods to extract foggy areas from WRF-RTFDDA forecasts using the satellite imagery. Since this is a problem of binary classification, we considered gradient boosted tree (GBT), random forest classification and Gaussian process methods. The experiments involved simulating 4 days of data. The data was divided into morning (06:00 LST to 09:00 LST) and night (01:00 LST to 04:00 LST) segments for each day. The model used 3 days of data for training and predicted the remaining day. This was repeated 4 times with different combinations of training and testing days. Each training set had about 400,000 values in total, which means 35,424 values (total number of grid-boxes inside the finest WRF-RTFDDA domain) per hour. The performance of random forest and Gaussian process methods highly depends on the size of the array of the training data; in this specific case Gaussian prediction fails to finish the training even for one hour data. The performance of

random forest also strongly depends on the size of the training dataset, therefore despite the method being suited well for analyzing ordered datasets, the GBT algorithm was chosen due to its performance.

The GBT algorithm was trained in order to determine if the WRF-RTFDDA forecast pixel belongs to the foggy area, or to the clear sky. The values of $T-T_d$, RH and WS (either at 1000 or 975 hPa) were used as features, and 0 and 1 were used as labels for clear and foggy pixels on EUMETSAT imagery, respectively. Results of this algorithm are shown and discussed in section 3.2.1.2.

2.2.5 Micro-physical analysis

The cloud-physics properties of fog events, like other aerosol phenomena, are usually described by the droplets size distribution. The effective radius, r_{eff}, is a weighted mean radius of droplets population and is calculated directly from the measured droplet-size distribution in the form (Hansen and Travis, 1974):

(1) $$r_{eff} = \frac{\int r^3 n(r) dr}{\int r^2 n(r) dr}$$

where r is the droplets radius and n is the number of droplets per unit volume. The LWC can also be calculated directly from the droplet size distribution as (Hansen and Travis, 1974):

(2) $$LWC = \frac{4}{3}\pi\rho \int r^3 n(r) dr$$

where ρ is water density.

The size distribution of droplets in fog has been extensively studied. (Deirmendjian, 1969) proposed commonly accepted typical density of size distributions of fog, describing the size distribution by a main mode around radii of 2-4 microns. The size distribution of fog droplets varies depending on the location. Local fog measurements reported in the literature describe specific and unique local fog parameters with a wide range of size distribution.

Among the variety of local fog measurements worldwide, only a few records characterize Israeli fog visibility, droplets sizes and concentration. Measurements performed in Tel Aviv (Ganor et al., 1993) found that 48-70% of the fog droplets were smaller than 1 µm. Two cases of heavy fog in Israel are reported in (David et al., 2013), followed by visibility ranges of 30 - 70 m, and fog concentration of 0.5-0.8 gr / m^3. The scarcity of reliable measurements held in Israel and the previously incomplete data turn our measurements and analysis into the first fully investigated and characterized fog event in Israel, in its synoptic, mesoscale and physical properties.

3. Results

3.1. Synoptic conditions

Figure 3 shows sea level pressure (SLP, contour lines) maps over the eastern Mediterranean at 00:00 UTC during January 3-6, 2021. The geographic domain roughly overlaps with that used by (Saaroni et al., 2020). The four panels show slightly different patterns of Red Sea Troughs. All of them are characterized by very weak north-easterly to easterly flow over Israel, as confirmed by 1000 and 925 hPa wind vectors in Figs. 5 and 6, respectively. These are inactive RSTs as no trough is present at 500 hPa above Israel (Fig. 4). Those synoptic conditions are favorable for fog development. Relative humidity presented in Figs. 5 and 6 at 1000 and 925 hPa as shaded contours reveal high levels at 1000 hPa, needed for fog development that drops at 925 hPa, enabling the development of fog at the first hundreds of meters above ground level only.

[Figure 3]

[Figure 4]

[Figure 5]

[Figure 6]

The automatic semi-objective classification following Alpert et al., (2004) classifies these events according to the 12 UTC NNRP reanalysis maps of geopotential height, winds and temperature and 1000hPa as RST with eastern axis for January 3, 2021 and RST with western axis for January 4-6, 2021.

3.2. Mesoscale analysis

3.2.1. Horizontal temporal evolution

3.2.1.1 Regional satellite-imagery of the fog event

Figure 7 most left panels displays RGB images of fog/low clouds for January 6, 2021, at night. The three panels summarize the formation of the fog over Israel including the area of our measurements and provide information about the drop sizes. At 00:00 UTC fog/low clouds developed mostly in the southern coast and limited inland areas, leaving the rest of the sea and land region clear. The colors over the covered areas represent warm, thick fog with small droplets. Areas surrounding the measurement site area are unevenly covered. At 02:00 UTC (Fig. 7) the covered area spread north of Tel-Aviv more distinctly, including the in-situ

measurements site. At 04:00 UTC (Fig. 7) the covered area spreads northwards and onto the sea, some southern patches are cleared, and the in-situ measurement area shows coverage. The development of the fog from south to north is a result of the land surface temperature being colder at arid areas in the south during nighttime. At 06:00 UTC (Fig. 8) the horizontal spread of the covered whole area is similar to the 04 UTC. At 08 UTC almost the entire area above Israel is clear caused by the sun heating. Similar behavior can be seen also in Figs. 13-15, Supporting material.

3.2.1.2 TA and GBT post-processing of WRF-RTFDDA for fog-conditions forecasts

Here we present the results of the TA and GBT algorithms described in sections 2.2.3 and 2.2.4.2.

Figures 7 and 8 show from left to right: (a) Column 1: EUMETSAT imagery ("natural_color" or "night_fog" composite for day or night, respectively) ; (b) Columns 2, 3, 4: T-T_d, RH and WS within the TA thresholds, respectively; (c) Column 5: Fog identified by the TA algorithm; (d) Column 6: Fog identified by the GBT algorithm; for night (00:00, 02:00 and 04:00 UTC) and day conditions (06:00 and 08:00 UTC) respectively, for January 6, 2021. Blue and red colors distinguish between identified areas over the sea and land, respectively. Figures for the rest of the days are presented in the Supporting Materials, Figs. 1-6 For night hours, the fog patterns produced by the TA and GBT algorithms are similar and resemble satellite imagery. However, both algorithms overestimate fog above the sea surface. Additionally, the TA algorithm underestimates foggy areas in the southern regions, while the GBT algorithm slightly overestimates fog over land (e.g. at 04:00 UTC). Despite this, the visual similarity between the GBT fog and satellite images is better than that between the TA and satellite fog.

[Figure 7]

From 08:00 UTC onwards, fog disappeared from the EUMETSAT imagery, but the fog-free zone was wrongly marked as fog by the GBT algorithm (Fig. 8 and Figs 4-6 from Supporting Materials). The shape of the GBT-derived fog depended on the land elevations; its boundary followed the elevation isolines, because the training features (temperatures, relative humidity and wind speed) varied similarly with altitude. For morning hours, the GBT algorithm shows overall better results than the TA. Similar to night hours, the TA underestimates fog above land, especially in Figs. 4-5 in the Supporting Materials. For example, in Fig. 4, at 06:00, the TA fog is almost absent while the GBT fog nicely matches the EUMETSAT-identified fog. During morning hours, the GBT algorithm wrongly identifies fog areas in the Eastern Negev (Fig. 8, distribution of ML predicted fog, column 6, the eastern part of the map) despite that the difference in temperatures is relatively big (Fig. 8, maps of T- T_d, column 2, for similar cases and precise values for T-T_d refer to the Supporting Materials, sections 2 and 4). Inspection of the areas

corresponding to the TA thresholds of T-T_d, RH and WS (columns 2, 3 and 4) reveals that a combination of the TA and GBT algorithm could provide optimal results. If an area is defined as fog by the GBT, but the values of T-T_d, RH and/or WS do not correspond to the TA thresholds; such areas should require additional scrutiny by the algorithm and/or be not considered as fog areas. Such a procedure applied for the Eastern Negev area, where GBT overestimation is the biggest, would provide improved fog-identification results.

Both, the satellite imagery and the model derived fog show gaps near the coastal metropolitan areas, this phenomenon might correspond to the urban heat islands, which eliminate fog areas by heating.

While the satellite imagery cannot distinguish between surface fog and low level clouds, the post-processed model does show differences between the two levels, providing the possibility of determining the vertical extent and level of the phenomenon.

[Figure 8]

3.2.2. Vertical extent analysis

In Fig. 9 we can see the vertical profiles of wind, dew point temperature, temperature, mixing ratio and relative humidity, as measured by the radiosonde (continuous lines and vectors) and scattered circles and vectors for the forecasts by WRF-RTFDDA on January 5, 2021, at 23:00 UTC. A low layer with high values of relative humidity, water vapor mixing ratio, calm winds, and very close values of temperature and dew-point temperature appears in both, forecast (up to ~300 m AGL) and radiosonde (up to ~250 m AGL). These are suitable conditions for radiation fog development. The model shows good agreement with the observations except for the intermediate level at about 500 AGL, indicating that more vertical model levels are probably needed to forecast the sharp changes along the vertical profile.

[Figure 9]

Vertical profiles for these parameters for the rest of the days can be found in the Supplementary Materials, Figs. 15-18. For January 4, 6, and 7, 2021 at 23:00 UTC (Figs. 16-18 from Supporting Materials) the difference between the temperature of the air and the dew point temperature in the low air layer is too large for fog development at Bet-Dagan station location. However, for January 3, 2021, at 23:00 UTC (Fig. 15 from Supporting Materials) the dew point temperature values are close to the air temperature, values of the relative humidity and water vapor mixing ratio are large enough, therefore, fog can be developed under these

conditions at Bet-Dagan location. Since fog developed at the Bet-Dagan station according to satellite imagery and model during all the analyzed days, we may conclude that conditions in the vertical profile probably developed later than the radiosondes launching time.

In addition to the radiosondes and model forecasts profiles in Fig. 9, Fig. 10 presents forecasts of time-cross sections of the vertical profile (on pressure levels) of RH, and WS in panel (a) and of T- Td and wind vectors in panel (b) at the Beit Dagan location. Following the TA thresholds defined for fog formation in section 2.2.3, we see that at Beit Dagan fog formed from the surface up to a height of 950 hPa after midnight, decreasing to a height of about 975 hPa before morning hours. After 06:00 UTC the lower levels near the surface are no longer prone to fog formation anymore, leaving low-level clouds as observed in the satellite imagery. This roughly coincides with the increase in visibility in the nearby measurements (see Fig. 12).

[Figure 10]

3.3. Micro physical analysis

The local meteorological properties of the fog event are shown in Fig. 11, including temperature, humidity, and winds, emphasizing that during the 4 consecutive nights, the fog started after midnight and vanished in the late morning. The characterized meteorological conditions for stable fog are relative humidity close to 100% and relatively low air temperatures (10-21 ^{o}C). Observed westerly winds (from the Mediterranean Sea direction) were weaker than 2 m/s along the whole fog event (not shown in that figure). Our former work concerning remote sensing measurements of the fog event (Tzadok et al., 2022) showed that the fog was not advected into the area but developed locally..

[Figure 11]

Fig. 12 follows the 6th, January 2021 morning, which may serve as a typical presentation of the fog conditions during the whole event, showing the measured visibility range, droplets size distribution, along with temperature and relative humidity. The fog event was characterized by minimum visibility of ~90 m. Droplets were characterized by main mode diameter of 1 to 2 μm, and an additional mode of about 6 μm. Fog started dissipating at about 09:50 LT after which relative humidity significantly decreased, visibility range increased, and large droplets disappeared.

[Figure 12]

The changes in the droplet sizes are well reflected also in the effective radius, calculated according to Eq. (1) and presented in Fig. 12(c). The effective radius is around 2 μm for the dense fog stage and growing slower toward 1 μm at the dissipation stage. Also shown in Fig. 12

is the LWC calculated according to Eq. (2). LWC was found to be around 0.005 g/m^3. Along with the fog event, its dissipation is followed by decreased LWC.

To compare this specific fog event in Israel with its observed properties to other fog events worldwide, we can refer to fog micro-physical properties that are discussed in detail by (Gultepe et al., 2007). They suggested that fog droplets are usually a composition of micron-size haze (unactivated) particles and activated droplets reaching tens of microns in size, with significant variability in the droplet size distribution. The resulting LWC are typically 0.01 - 0.4 g/m^3. According to (KOCMOND WC and PERCHONOK K, 1970), the average radiation fog drop diameter is 5 μm while the typical droplet size range is 2.5-17.5 μm and LWC is 0.11 g/m^3 with typical horizontal visibility of 100 m. Bi-modal distributions are also known in the literature, for example, (Podzimek, 1997), with a dominant volume mode of droplets radius of about 10 µm and a much smaller mode of 2.5-5 µm.

Thus, the January fog droplets seem to be relatively small. Their size ranges are in accordance with very low LWC, followed by relatively high visibility ranges.

4. Summary

A rare and dense regional-scale radiation-fog event served as a case study for analyzing fog characteristics in Israel. The event was studied using in-situ measurements for micro-physical analysis, NCEP/NCAR reanalysis to determine the synoptic conditions, EUMETSAT imagery to analyze the 2-dimensional spatio-temporal evolution and radiosondes to investigate its vertical extent. Post-processing of WRF-RTFDDA forecasts served to analyze the 3-dimensional spatio-temporal evolution and the ability to forecast the event.

The in-situ measurements showed that the visibility range was as low as 90 m and that the main mode of droplet size was of 1-2 microns, followed by another mode around 6 micrometers. Typical LWC values were in the range 0.01-0.025 g/m^3. These values represent fog with tiny droplets and low liquid water contents.

During the four days of the event, the area was influenced by a ‘dry’ Red Sea Trough synoptic system with very weak north-easterly to easterly winds, favorable for radiation-fog development.

EUMETSAT IR and visible imagery enabled tracking of the spatio-temporal development of the regional fog event from south to central coastal areas and its dissipation at morning hours. The in-situ measured droplet size distribution agrees with the identification of the satellite images as small-drop fog.

Fog forecasting using numerical weather prediction models is still challenging, as microphysics parameterizations are crude in their representation of fog. Therefore, we used two algorithms based on basic model prognostic variables, wind speed, dew-point temperature, and relative humidity, as is frequently done in operational forecasting systems. Post-processing of WRF-RTFFDA forecasts with a simple thresholds-based algorithm (TA) and an GBT ML algorithm proved useful to identify fog areas. The GBT algorithm over-performed the TA algorithm during early morning hours, though it overestimates fog areas during the late morning. The combination of the GBT algorithm and TA can remove this inaccuracy providing an optimal strategy to post-process model forecasts.

Detailed analysis of the fog events shows that the WRF-RTFDDA post-processed forecasts at 1-km grid size overall succeeded in predicting the temporal and spatial evolution of the dense fog. Yet, some differences are noted, particularly as landuse characteristics used in the present forecasting system rely on WRF model system data that has not been updated for the past decades. Moreover, the WRF-RTFDDA forecasts enable distinguishing between near-surface fog and elevated fog/low level clouds, a characteristic that cannot be deduced from satellite images. Clear patches appear in both satellite imagery and WRF-RTFDDA forecasts, in particular, over coastal areas characterized by urban landuse and subsequent heat-island effect at night. Similar phenomena have been observed in other areas around the globe.

Since WRF-RTFDDA forecasts were initialized at 18 UTC and made available after a few hours run, they provided real time forecasts ahead of time. They proved the usefulness of the system in forecasting this massive fog and low clouds event and in providing alerts to users.

In summary, the unprecedented comprehensive analysis presented here describes the fog event in all its aspects. Starting from the synoptic conditions that support fog formation, high-resolution spatial and temporal meteorological model (post-processed by thresholds-based and machine-learning algorithms) for the prediction of its extent, and validation through satellite remote-sensing and in-situ ground measurement of the actual physical properties of the fog. The two main conclusions and findings from our research are:

1. Microphysical data about fog in Israel associated with a complete meteorological and synoptic analysis. This is the first time ever that such reliable and prolonged data has been acquired, and it fills the noticeable gap that was present in our area.

2. We have shown that we can use a meteorological model for fog forecast in our area in order to provide alerts and to plan an early deployment of instrumentation at the fog prone locations at appropriate times. This fact will assist us to deploy future measurement campaigns to fully characterize the microphysical properties of different

fog events (both in terms of synoptic conditions and geographic locations) and provide the essential link between the two.

Open Research

The data used in current WRF simulations is delivered in grib format and was obtained (and available) from ECMWF model, MARS catalogue:

https://www.ecmwf.int/en/forecasts/datasets/search?f%5B0%5D=sm_field_dataset_urls_filter%3Afield_dataset_mars_url. Registration required.

EUMETSAT data includes 12 channels and their RGB composites “night_fog” and “fog” are available via EUMETSAT Data Ordering Application:

https://eoportal.eumetsat.int/. Registration required.

Weather Research and Forecast (WRF) model serves for numerical weather simulations, its source code (current version is 4.5) is available via the official WRF web page:

https://www.mmm.ucar.edu/models/wrf.

References

Alpert, P., Osetinsky, I., Ziv, B., Shafir, H., 2004. Semi-objective classification for daily synoptic systems: Application to the eastern Mediterranean climate change. Int. J. Climatol. 24. https://doi.org/10.1002/joc.1036

David, N., Alpert, P., Messer, H., 2013. The potential of commercial microwave networks to monitor dense fog-feasibility study. J. Geophys. Res. Atmos. 118. https://doi.org/10.1002/2013JD020346

Deirmendjian, D., 1969. Single Scattering on Many Particles. Electromagnetic Scattering on Spherical Polydispersions. Am. Elsevier Publ. Companym Inc. New York, NY, USA 77–83.

Eronn, A., 2007. Fog detection in cold winter situations at high latitudes, in: Final Report of EUMETSAT Graduate Trainee.

Erturk, A., Prieto, J., 2010. Detection of Fog / Low Stratus Using MSG SEVIRI Images. 5th Int. Conf. Fog, Fog Collect. Dew 1–2.

Ganor, E., Levin, Z., Pardess, D., 1993. Determining the acidity and chemical composition of fog, haze and cloud droplets in Israel. Atmos. Environ. Part A, Gen. Top. 27. https://doi.org/10.1016/0960-1686(93)90287-9

Goldreich, Y., 2003. The Climate of Israel, The Climate of Israel. https://doi.org/10.1007/978-1-4615-0697-3

Gultepe, I., Tardif, R., Michaelides, S.C., Cermak, J., Bott, A., Bendix, J., Müller, M.D., Pagowski, M., Hansen, B., Ellrod, G., Jacobs, W., Toth, G., Cober, S.G., 2007. Fog research: A review of past achievements and future perspectives. Pure Appl. Geophys. https://doi.org/10.1007/s00024-007-0211-x

Haeffelin, M., Bergot, T., Elias, T., Tardif, R., Carrer, D., Chazette, P., Colomb, M., Drobinski, P., Dupont, E., Dupont, J.C., Gomes, L., Musson-Genon, L., Pietras, C., Plana-Fattori, A., Protat, A., Rangognio, J., Raut, J.C., Rémy, S., Richard, D., Sciare, J., Zhang, X., 2010. PARISFOG: Shedding new light on fog physical processes. Bull. Am. Meteorol. Soc. 91. https://doi.org/10.1175/2009BAMS2671.1

Hansen, J.E., Travis, L.D., 1974. Light scattering in planetary atmospheres. Space Sci. Rev. 16. https://doi.org/10.1007/BF00168069

Huang, Y., Liu, Yubao, Xu, M., Liu, Yuewei, Pan, L., Wang, H., Cheng, W.Y.Y., Jiang, Y., Lan, H., Yang, H., Wei, X., Zong, R., Cao, C., 2018. Forecasting severe convective storms with WRF-based RTFDDA radar data assimilation in Guangdong, China. Atmos. Res. 209. https://doi.org/10.1016/j.atmosres.2018.03.010

Kalnay, E., White, G., Woollen, J., Chelliah, M., Fiorino, M., Kanamitsu, M., Jenne, R., Kistler, R., Saha, S., Kousky, V., Collins, W., Ebisuzaki, W., H, van den D., 2001. The NCEP-NCAR 50-year reanalysis: Monthly means CD-ROM and documentation. Bull. Am. Meteorol. Soc. 2.

Kim, M., Cermak, J., Andersen, H., Fuchs, J., Stirnberg, R., 2020. A new satellite-based retrieval of low-cloud liquid-water path using machine learning and meteosat seviri data. Remote Sens. 12. https://doi.org/10.3390/rs12213475

Kistler, R., Kalnay, E., Collins, W., Saha, S., White, G., Woollen, J., Chelliah, M., Ebisuzaki, W., Kanamitsu, M., Kousky, V., Van Den Dool, H., Jenne, R., Fiorino, M., 2001. The NCEP-NCAR 50-year reanalysis: Monthly means CD-ROM and documentation. Bull. Am. Meteorol. Soc. 82. https://doi.org/10.1175/1520-0477(2001)082<0247:TNNYRM>2.3.CO;2

KOCMOND WC, PERCHONOK K, 1970. HIGHWAY FOG. Highw Res Bd, Nat Coop Highw Res Progr. Rep 95.

Levi, W.M., 1967. Fog in Israel. Isr. J. earth Sci. 16, 7–21.

Liu, Y., Warner, T.T., Astling, E.G., Bowers, J.F., Davis, C.A., Halvorson, S.F., Rife, D.L., Sheu, R.S., Swerdlin, S.P., Xu, M., 2008. The operational mesogamma-scale analysis and forecast system of the U.S. Army Test and Evaluation Command. Part II: Interrange comparison of the accuracy of model analyses and forecasts. J. Appl. Meteorol. Climatol. 47. https://doi.org/10.1175/2007JAMC1654.1

Nilo, S.T., Cimini, D., Di Paola, F., Gallucci, D., Gentile, S., Geraldi, E., Larosa, S., Ricciardelli, E.,

Ripepi, E., Viggiano, M., Romano, F., 2020. Fog forecast using WRF model output for solar energy applications. Energies 13. https://doi.org/10.3390/en13226140

Owens, R.G., Hewson, T.D., 2018. ECMWF forecast user guide. Reading: ECMWF.

Papin, C., Bouthemy, P., Rochard, G., 2002. Unsupervised segmentation of low clouds from infrared METEOSAT images based on a contextual spatio-temporal labeling approach. IEEE Trans. Geosci. Remote Sens. 40. https://doi.org/10.1109/36.981353

Podzimek, J., 1997. Droplet concentration and size distribution in haze and fog. Stud. Geophys. Geod. 41. https://doi.org/10.1023/A:1023350917344

Raspaud, M., Hoese, D., Dybbroe, A., Lahtinen, P., Devasthale, A., Itkin, M., Hamann, U., Rasmussen, L.Ø., Nielsen, E.S., Leppelt, T., Maul, A., Kliche, C., Thorsteinsson, H., 2021. TOOLS: PyTroll: An open-source, community-driven python framework to process earth observation satellite data. Bull. Am. Meteorol. Soc. https://doi.org/10.1175/BAMS_997_1313-1336_NOWCAST

Ronen, A., Tzadok, T., Rostkier-Edelstein, D., Agassi, E., 2021. Fog measurements with ir whole sky imager and doppler lidar, combined with in situ instruments. Remote Sens. 13. https://doi.org/10.3390/rs13163320

Saaroni, H., Harpaz, T., Alpert, P., Ziv, B., 2020. Automatic identification and classification of the northern part of the Red Sea trough and its application for climatological analysis. Int. J. Climatol. 40. https://doi.org/10.1002/joc.6416

Skamarock, W.C.., Klemp, J.B., Dudhia, J.B., Gill, D.O., Barker, D.M., Duda, M.G., Huang, X.-Y.., Wang, W., Powers, J.G., 2021. A Description of the Advanced Research WRF Model Version 4.3, NCAR Technical Note.

Tzadok, T., Ronen, A., Rostkier-Edelstein, D., Agassi, E., Avisar, D., Berkovic, S., Manor, A., 2022. Profiling the Planetary Boundary Layer Wind with a StreamLine XR Doppler LiDAR: Comparison to In-Situ Observations and WRF Model Simulations. Remote Sens. 14. https://doi.org/10.3390/rs14174264

Figures

Figure 1. Field-experiment area map [Google maps] showing the measurement site in Ness Ziona and the meteorological stations nearby; (b) Droplet-sizes measurements [FSSP-100, PMS]; and (c) Visibility-range sensor [SWS250, Biral].

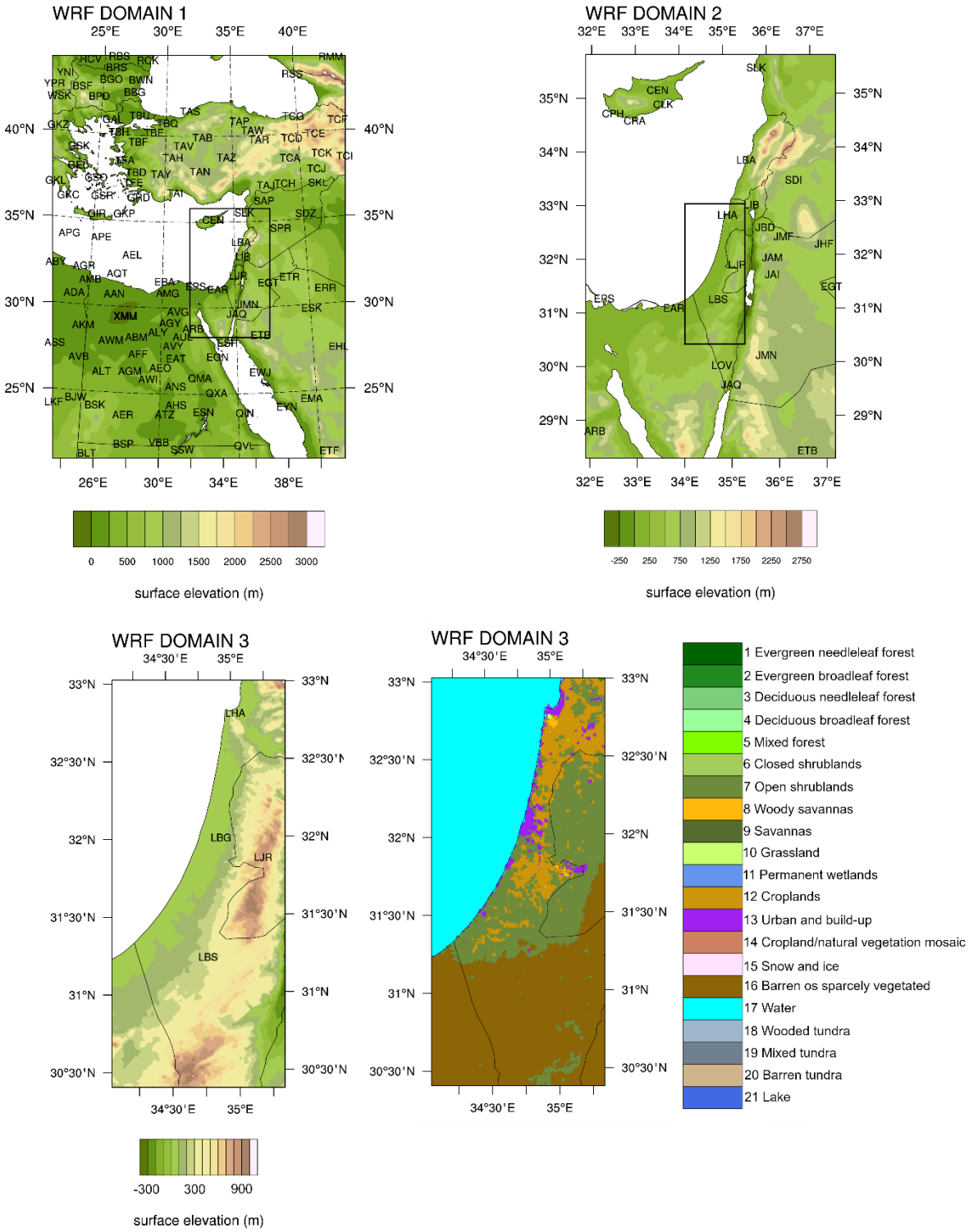

Figure 2. Nested WRF domains configuration: (a) domains D01 and D02; (b) domains D02 and D03; (c) domain D03; and (d) dominant landuse categories of D03 domain.

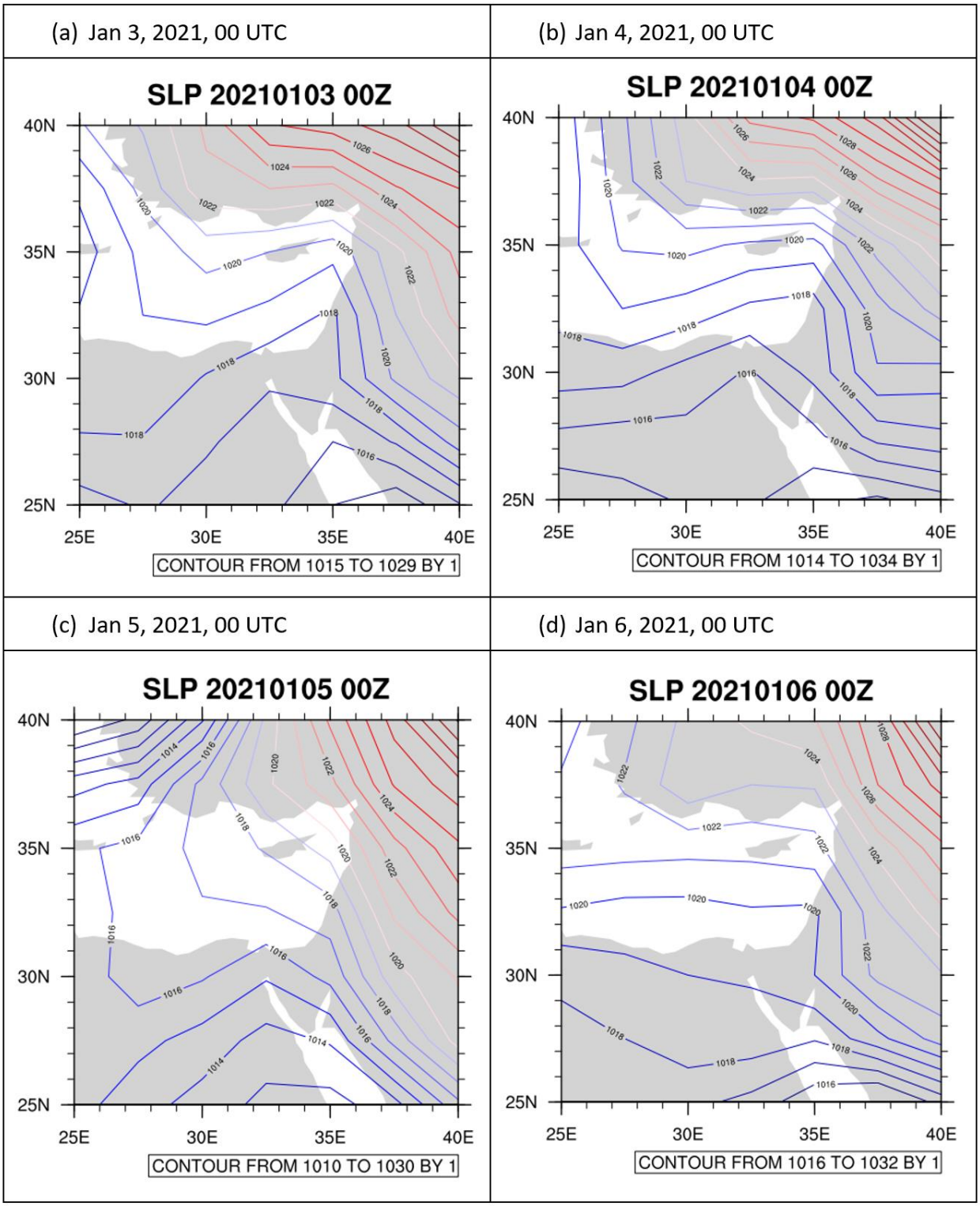

Figure 3. Sea level pressure (contours) over the eastern Mediterranean at 00 UTC during (a) 3rd of January; (b) 4th of January; (c) 5th of January; and (d) 6th of January 2021.

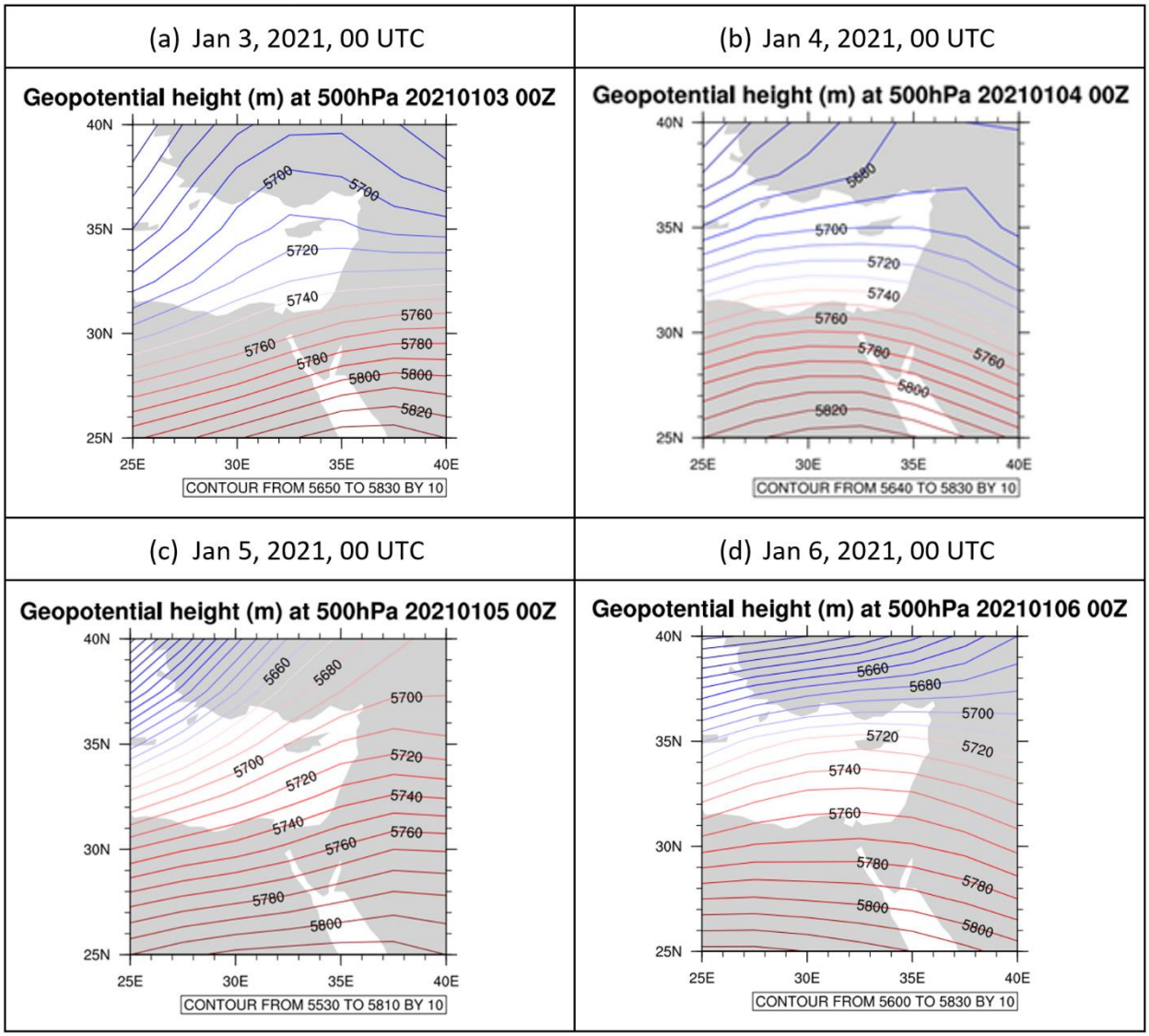

Figure 4. Geopotential height (contours) at 500hPa over the eastern Mediterranean at 00 UTC during (a) 3rd of January; (b) 4th of January; (c) 5th of January; and (d) 6th of January 2021.

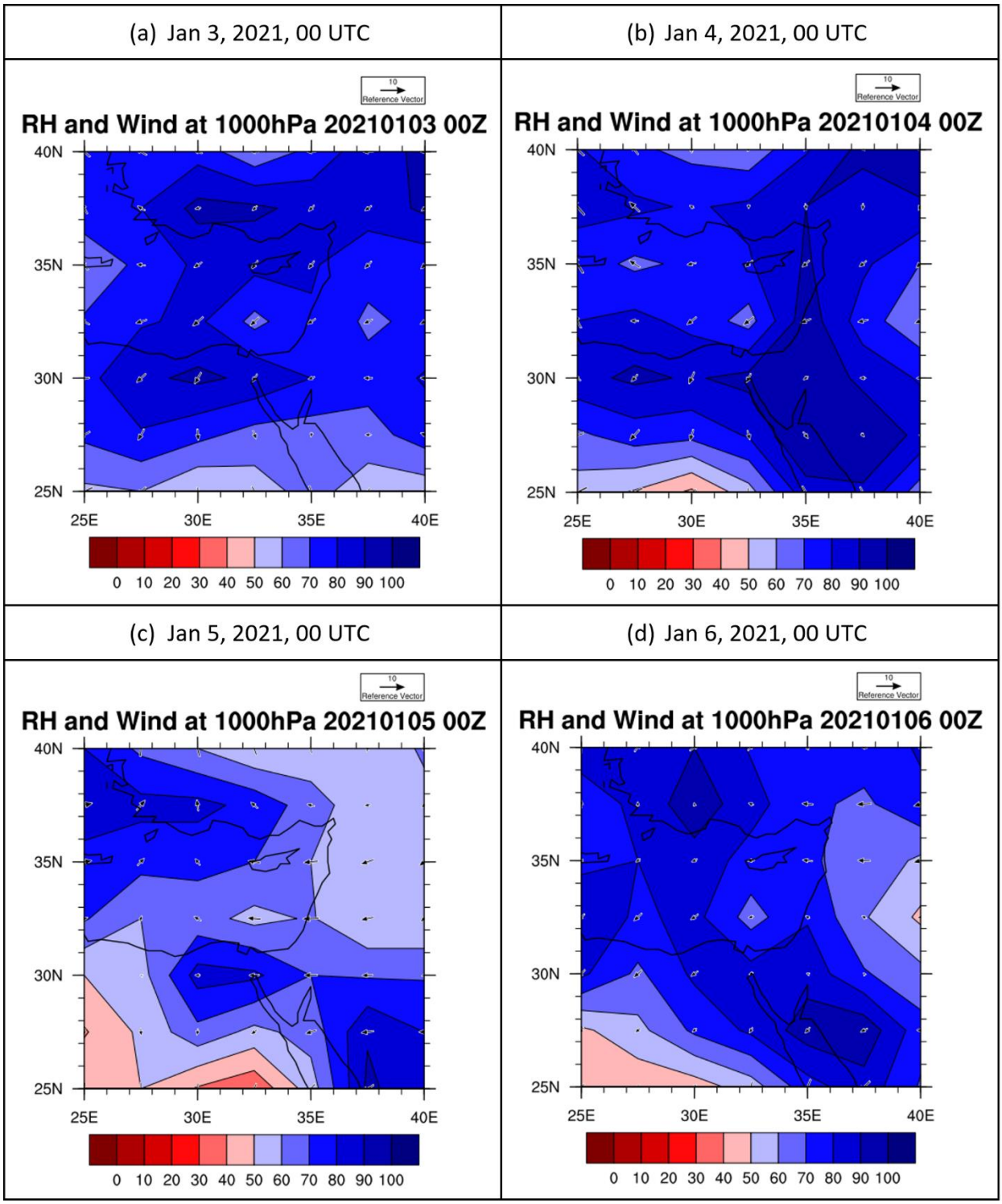

Figure 5. Relative humidity (shaded contours) and horizontal wind vectors at 1000hPa over the eastern Mediterranean at 00 UTC during (a) 3rd of January; (b) 4th of January; (c) 5th of January; and (d) 6th of January 2021.

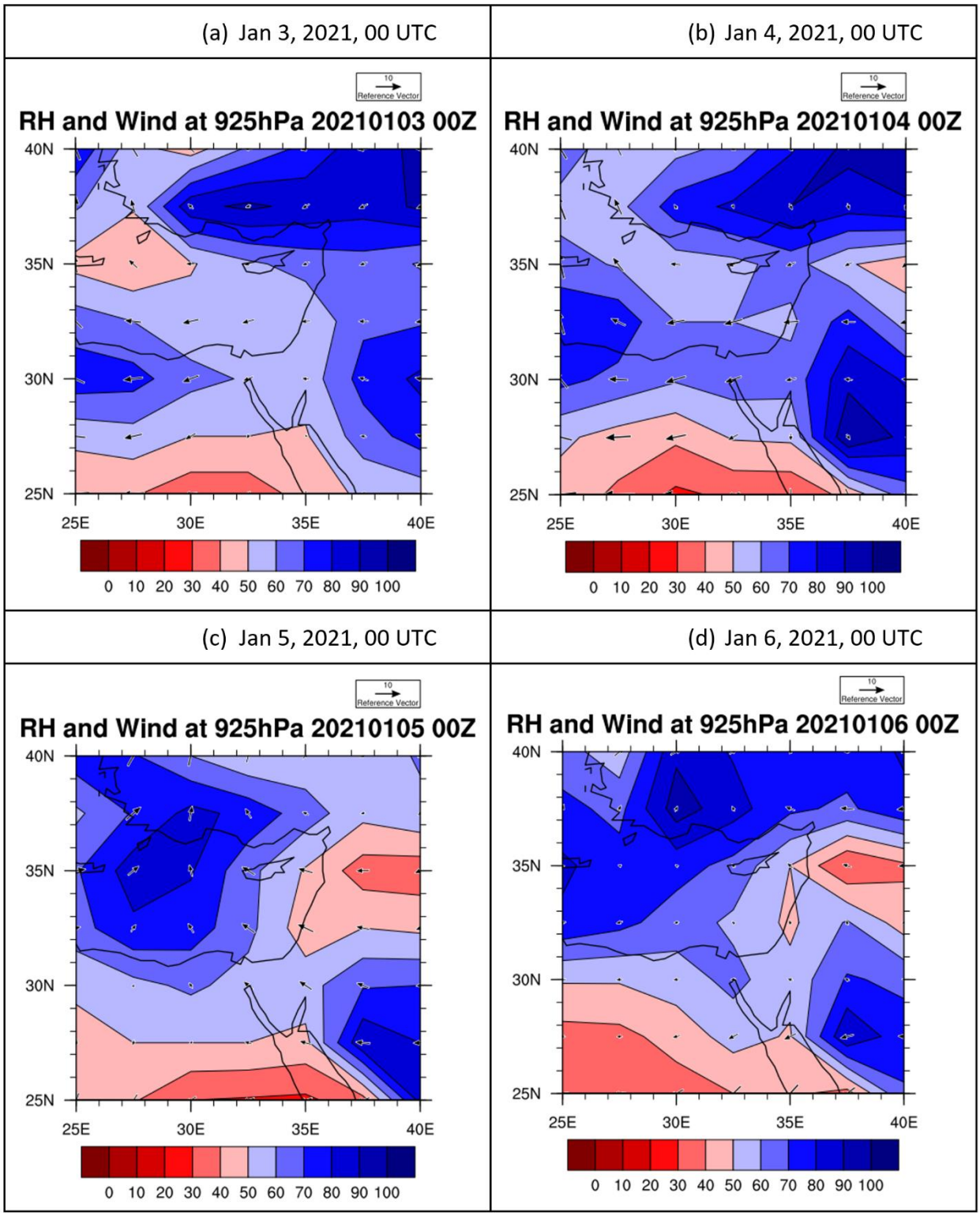

Figure 6. Same as Fig. 5 except at 925hPa

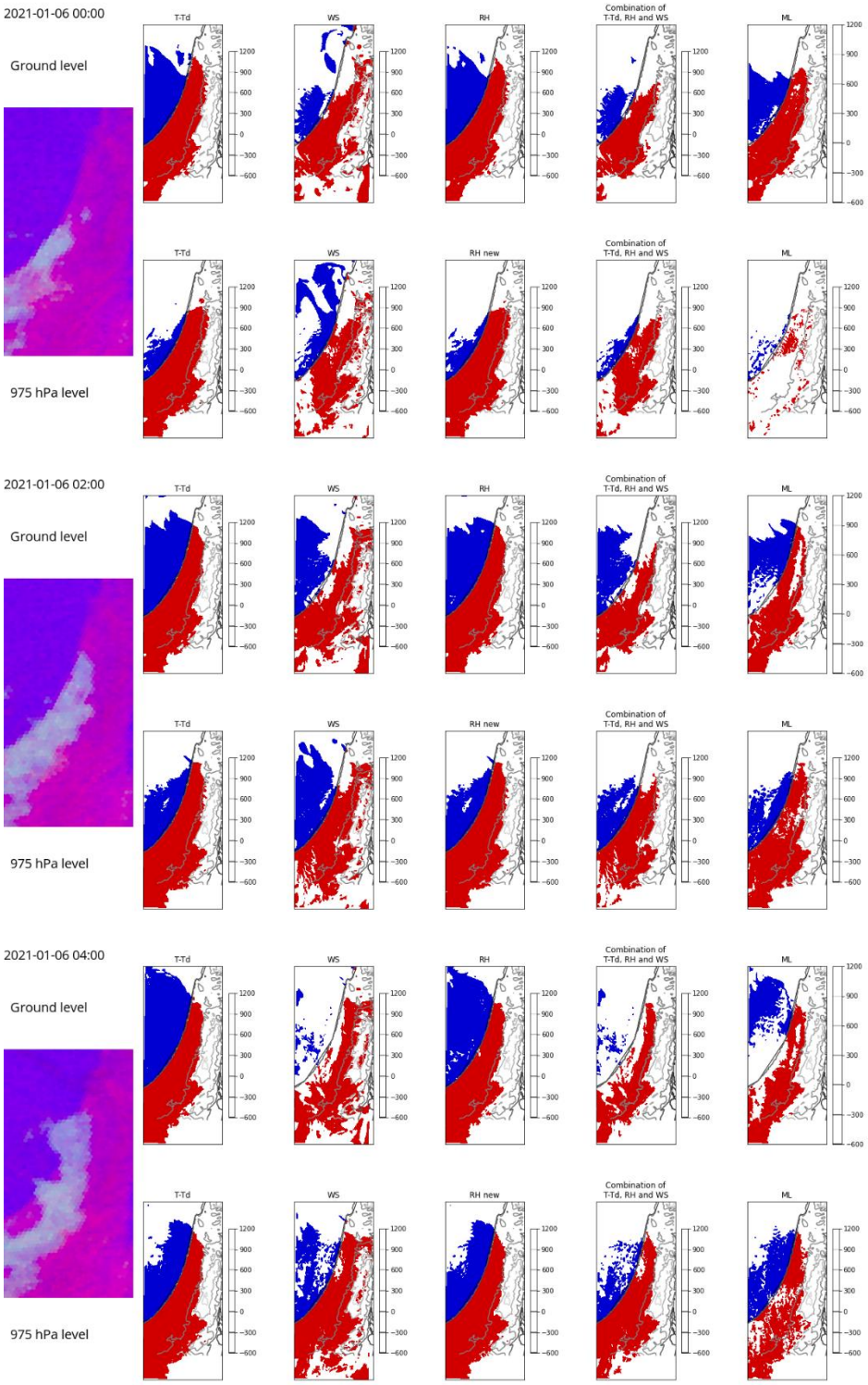

Figure 7. RGB images of fog/low clouds from EUMETSAT data (1st column from the left) for nighttime; maps from WRF model of T-Td, wind and relative humidity (2nd, 3rd and 4th columns from the left). The 5th column shows the overlap of T-Td with RH and WS. The 6th column is a GBT result.

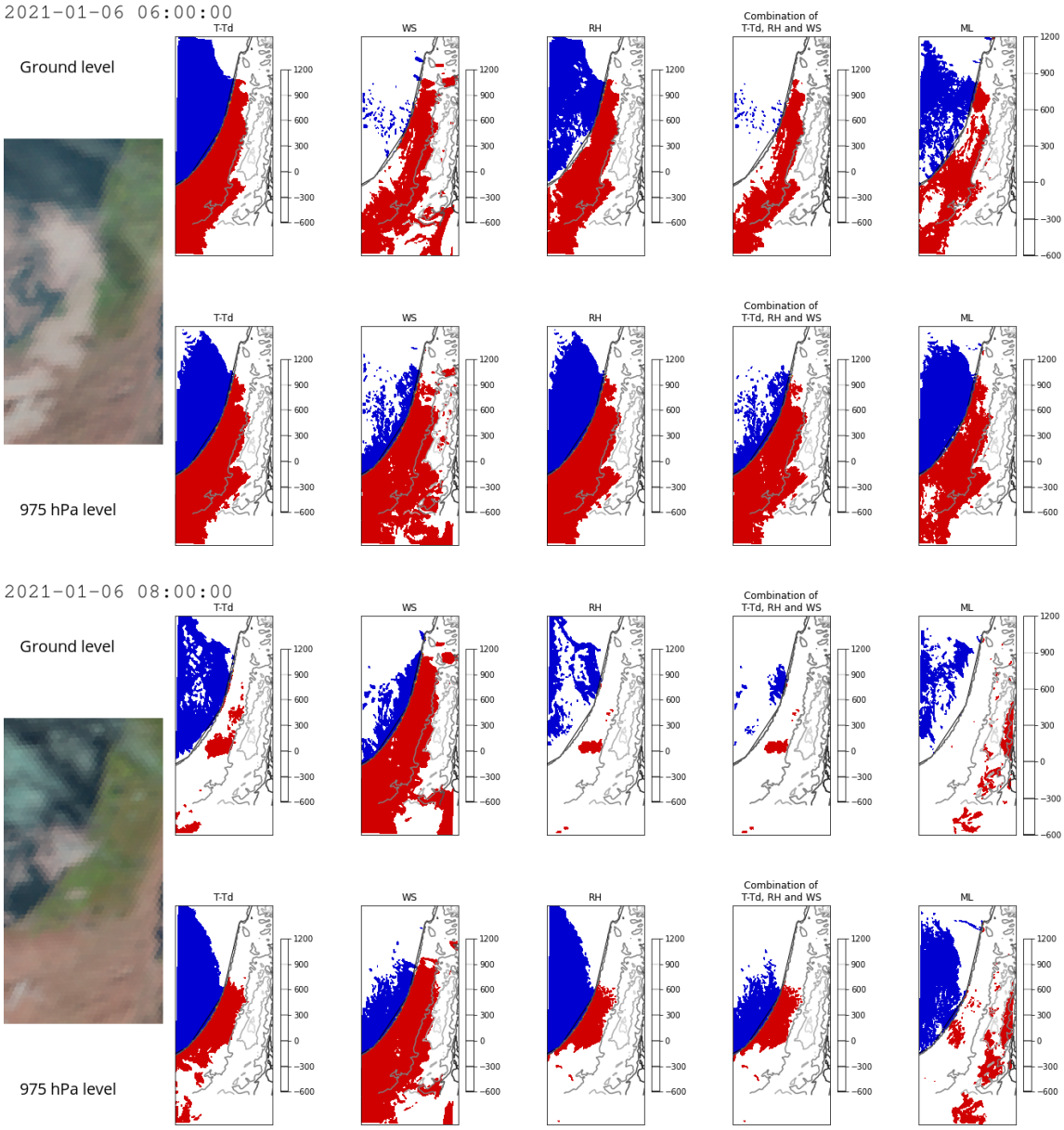

Figure 8. RGB images of fog/low clouds from EUMETSAT data (1st column from the left) for daytime; maps from WRF model of T-Td, wind and relative humidity (2nd, 3rd and 4th columns from the left). The 5th column shows the overlap of T-Td with RH and WS. The 6th column is a GBT result.

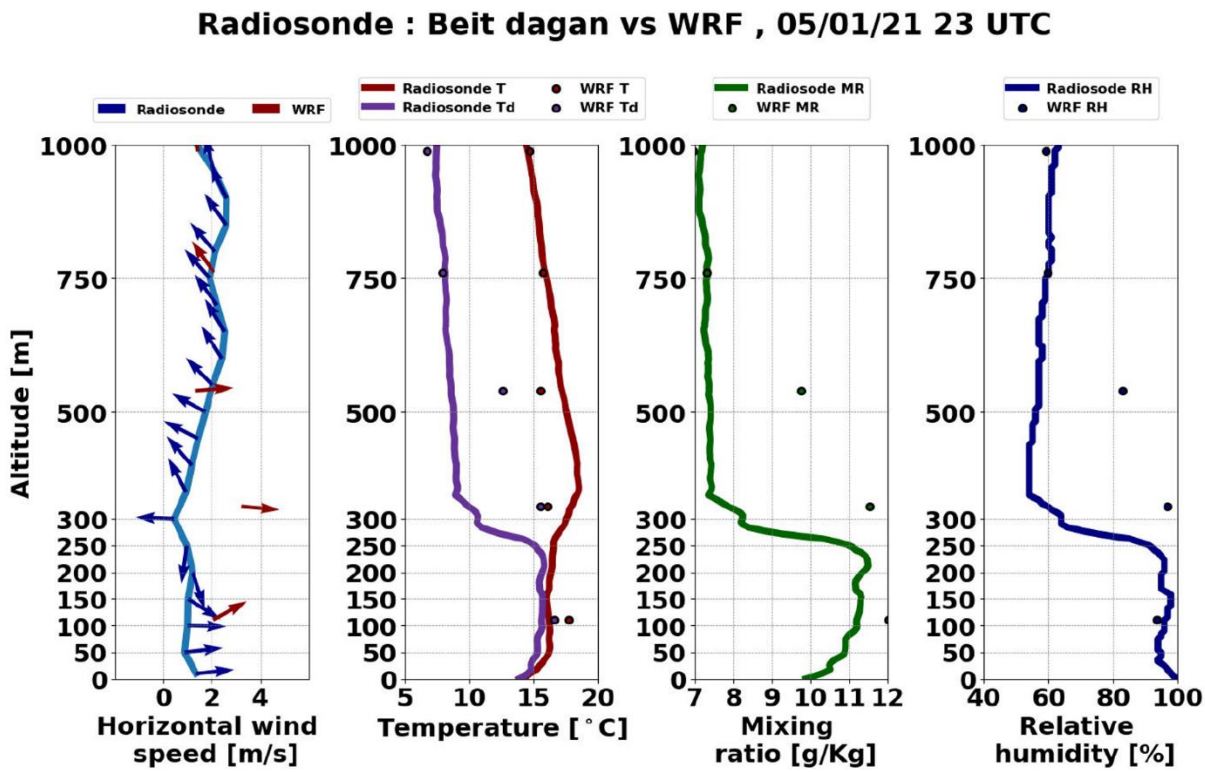

Figure 9. Vertical profiles of winds (arrows), temperature, dew point temperature, relative humidity, and mixing ratio of radiosonde on 5th of January 2021 23 UTC. Single symbols along the profiles represent the WRF-RTFDDA forecast values at the available vertical levels.

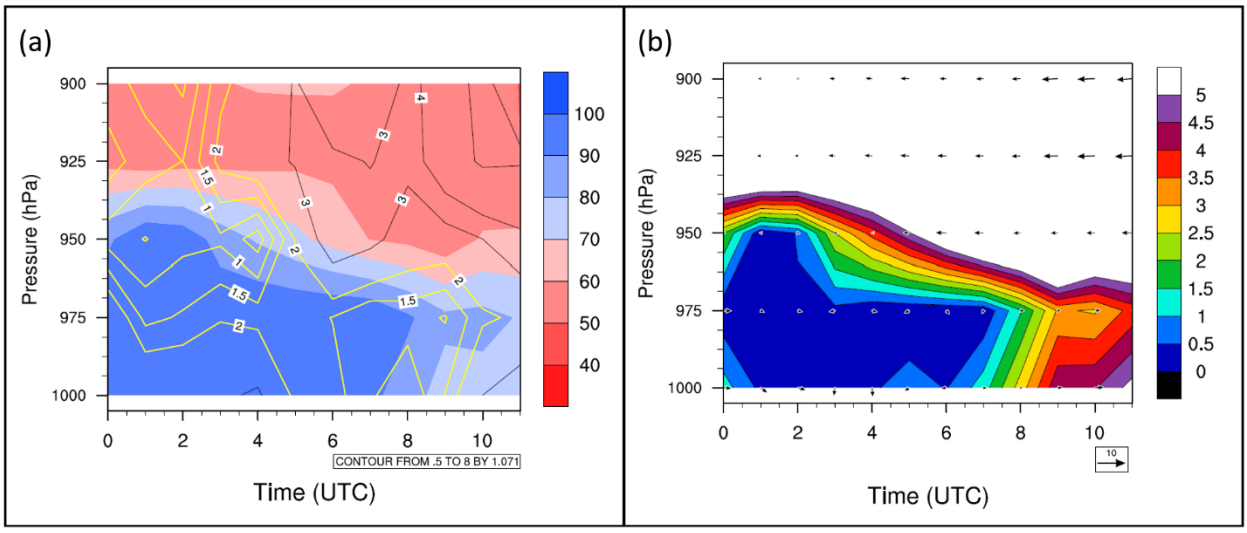

Figure 10. Forecasts of time-cross sections of the vertical profile (on pressure levels) of RH and wind-speed in panel (a) and of dew-point depression and wind vectors in panel (b) at Beit Dagan location. Wind speeds in units of m/s, RH as percentages and dew-point depression in units of Celsius degrees.

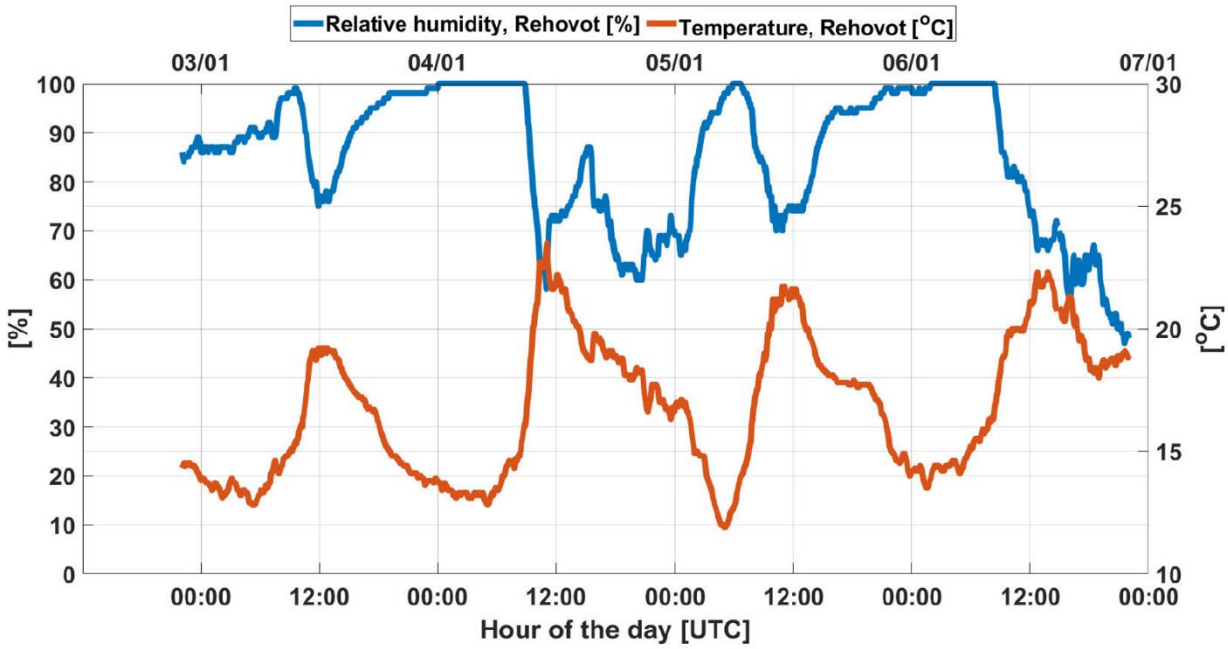

Figure 11. Relative humidity and air temperature during the January 2021 event, taken from "Rehovot" station. The x-axis time label denotes time- noon or midnight/date between 3rd-7th of January 2021.

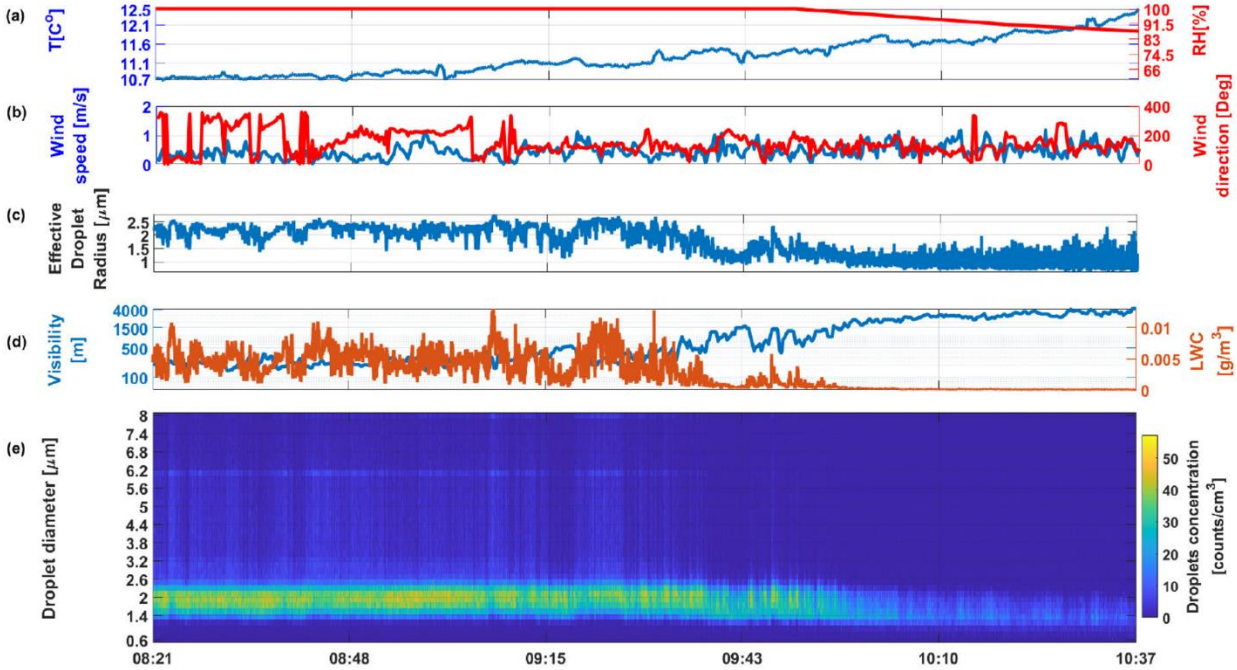

Figure 12. Fog evolution during the morning of Jan 6, 2021: (a) Temperature (Ness Ziona) and relative humidity (Beit Dagan); (b) Wind speed and wind direction (Ness Ziona); (c) Effective droplet radius; (d) Visibility range, and (e) Droplet size distribution

Figure 1.

© Google maps
Tel-Aviv
Tel Aviv-Yafo
Bnei Brak
Giv'at Shmu'el
SARONA
Ramat Gan
NEVE TZEDEK
Kiryat Ono
JAFFA
Sheba Medical Cent
Wolfson Medical Center
Or Yehuda
Azor
Holon
Beit Dagan
Bat Yam
Kfar Habad
NAHALAT YEHUDA
Rishon LeTsiyon
Tsrifin
Nir Zvi
Neta'im
Be'er Ya'akov
Bet Hanan
Palmahim
Ness Ziona
Irus, Israel
Nezer Sereni
Yashresh
Rehovot
The Mediterranean Sea
(a)
Imagery ©2021 TerraMetrics, Map data ©2021 Mapa GISrael Israel Terms Privacy Send feedback 2 km

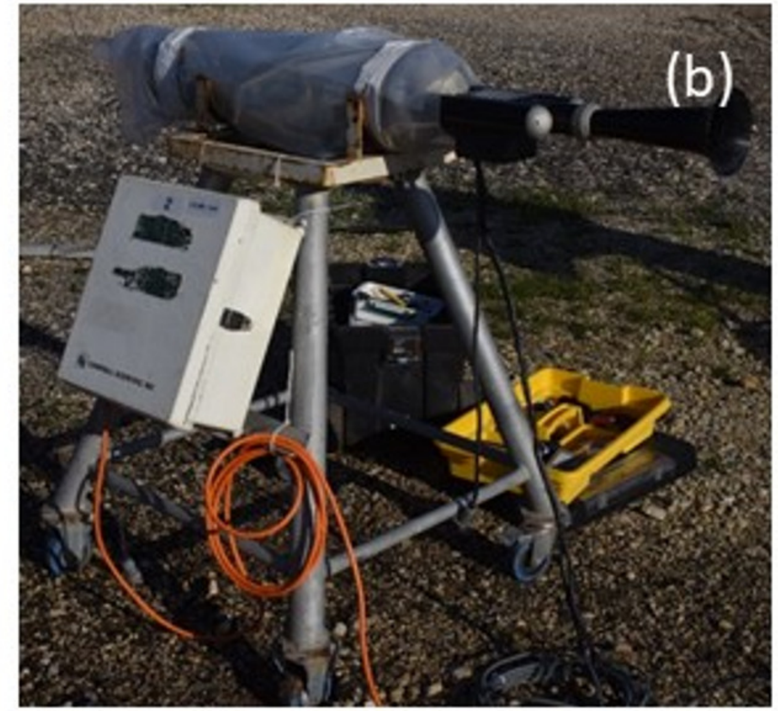
(b)

(c)

Figure 2.

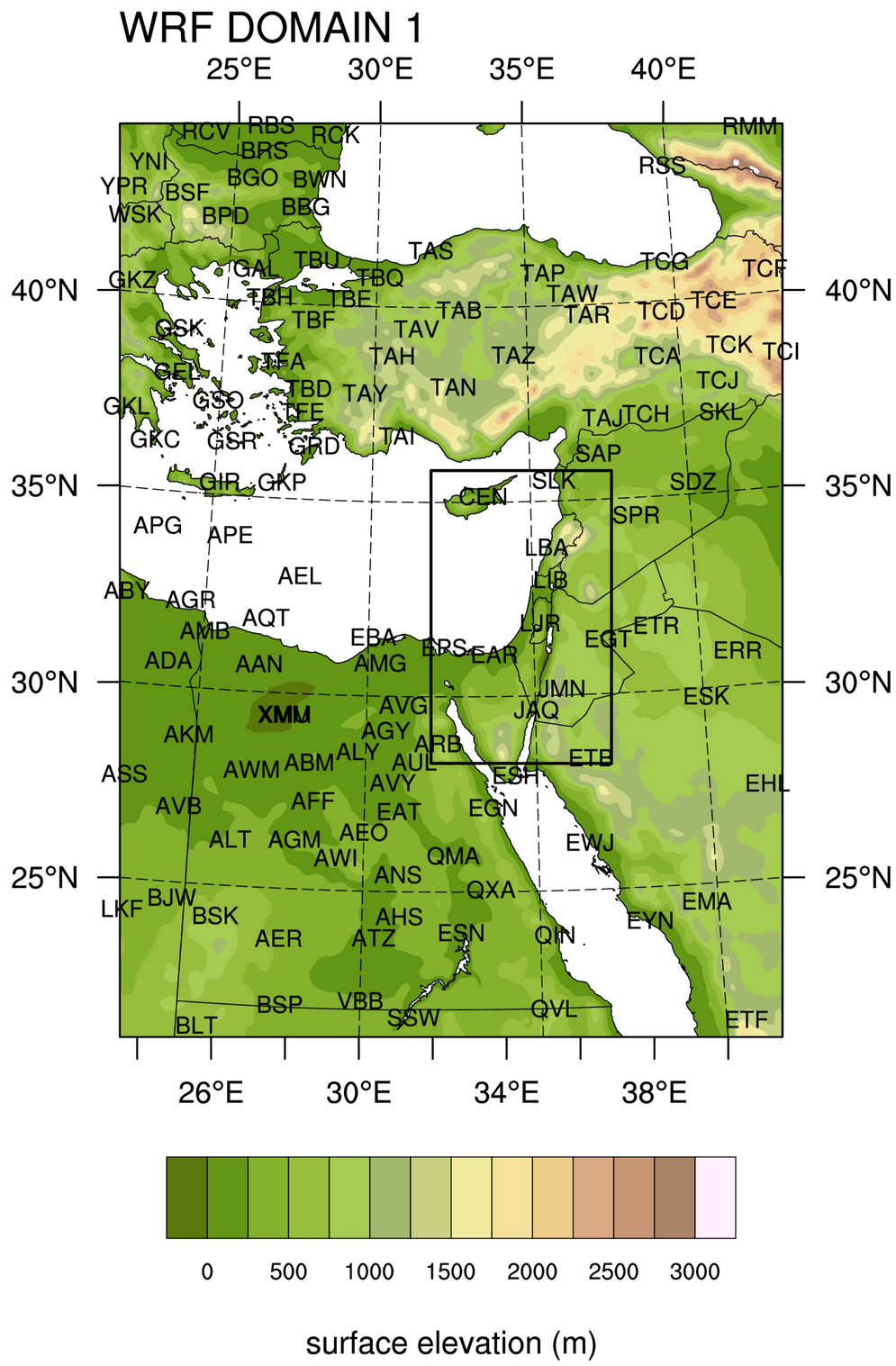
WRF DOMAIN 1
25°E
30°E
35°E
40°E
40°N
35°N
30°N
25°N
26°E
30°E
34°E
38°E
0
500
1000
1500
2000
2500
3000
surface elevation (m)

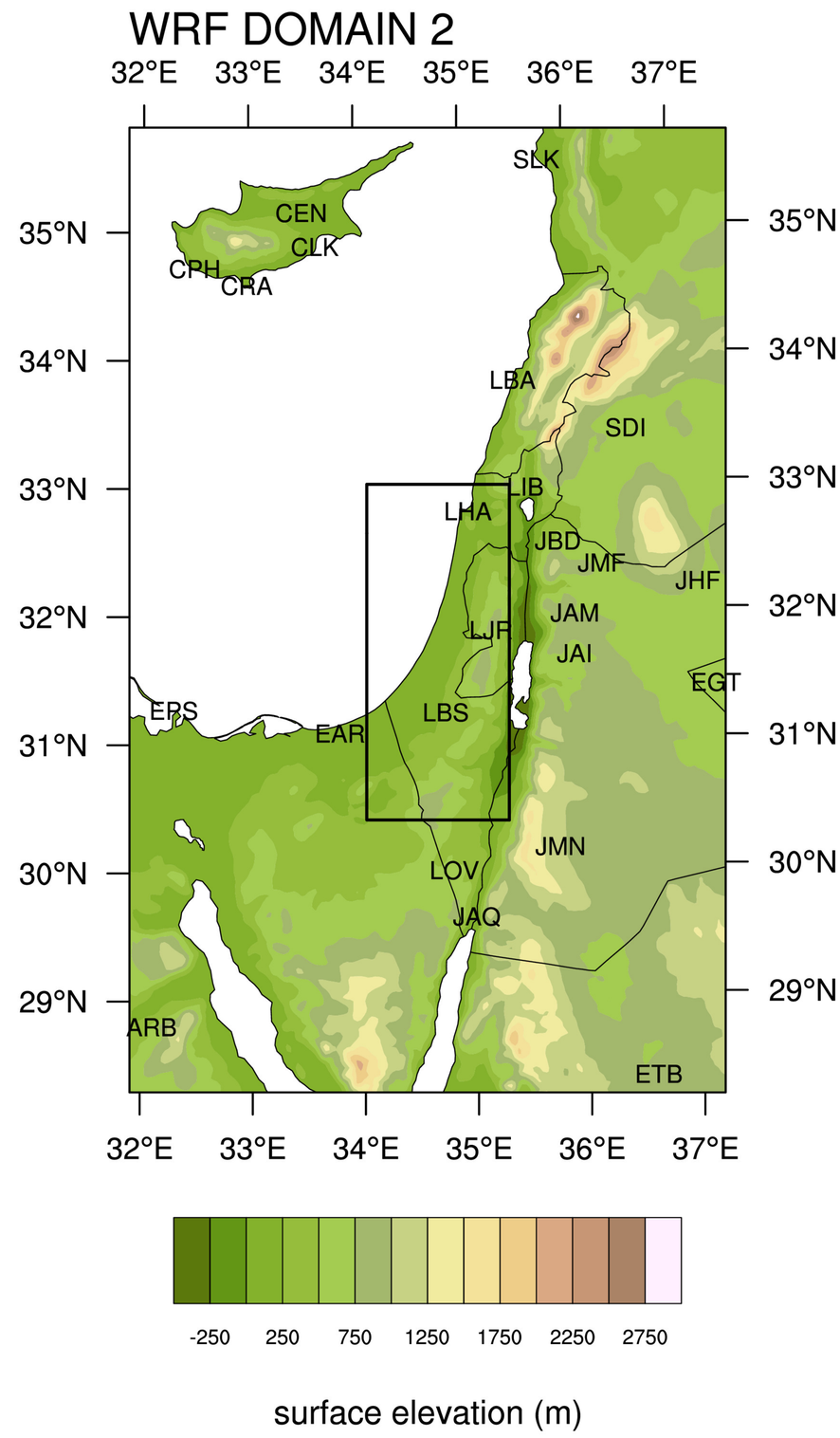
WRF DOMAIN 2
32°E
33°E
34°E
35°E
36°E
37°E
35°N
34°N
33°N
32°N
31°N
30°N
29°N
-250
250
750
1250
1750
2250
2750
surface elevation (m)

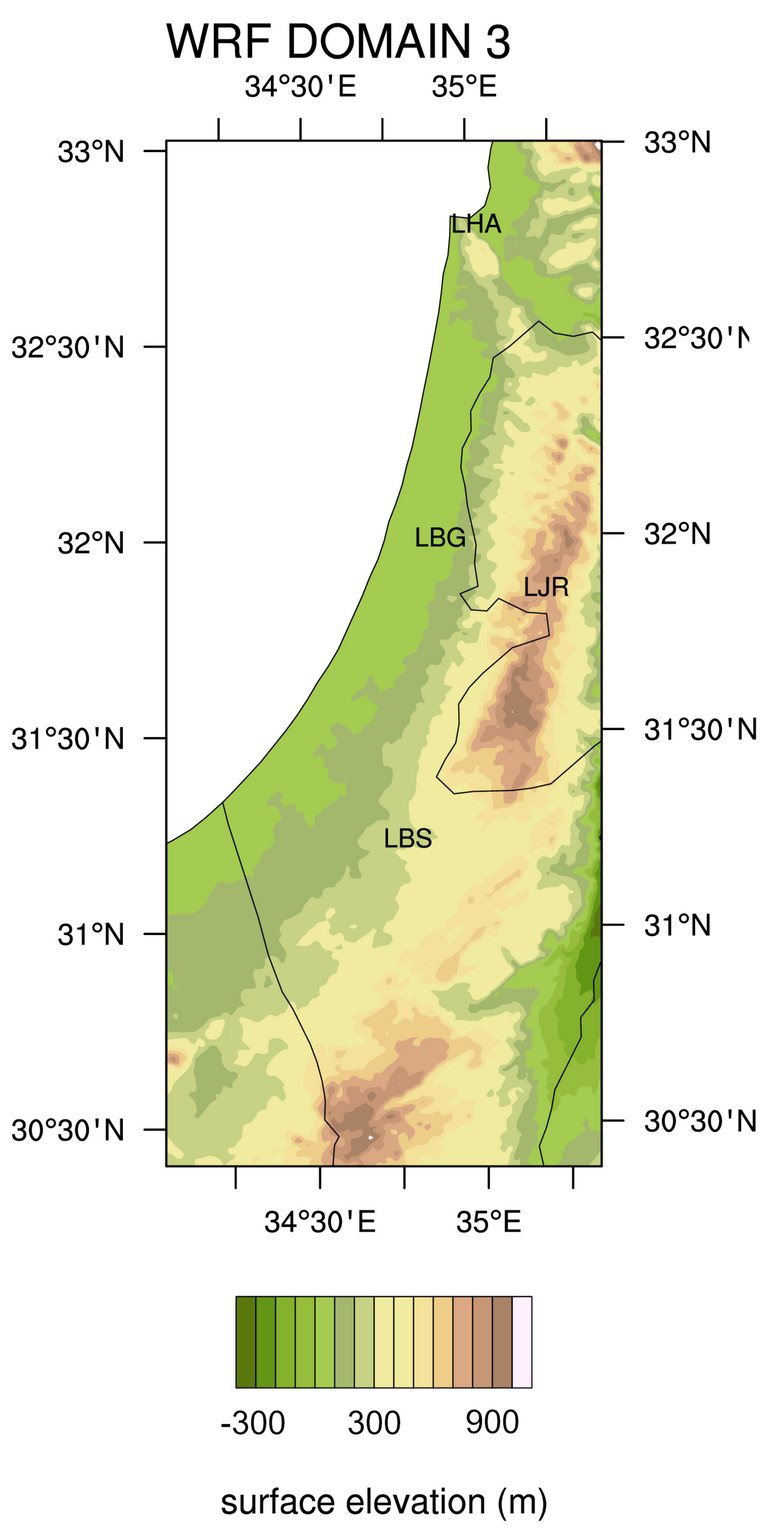
WRF DOMAIN 3
34°30'E
35°E
33°N
32°30'N
32°N
31°30'N
31°N
30°30'N
-300
300
900
surface elevation (m)

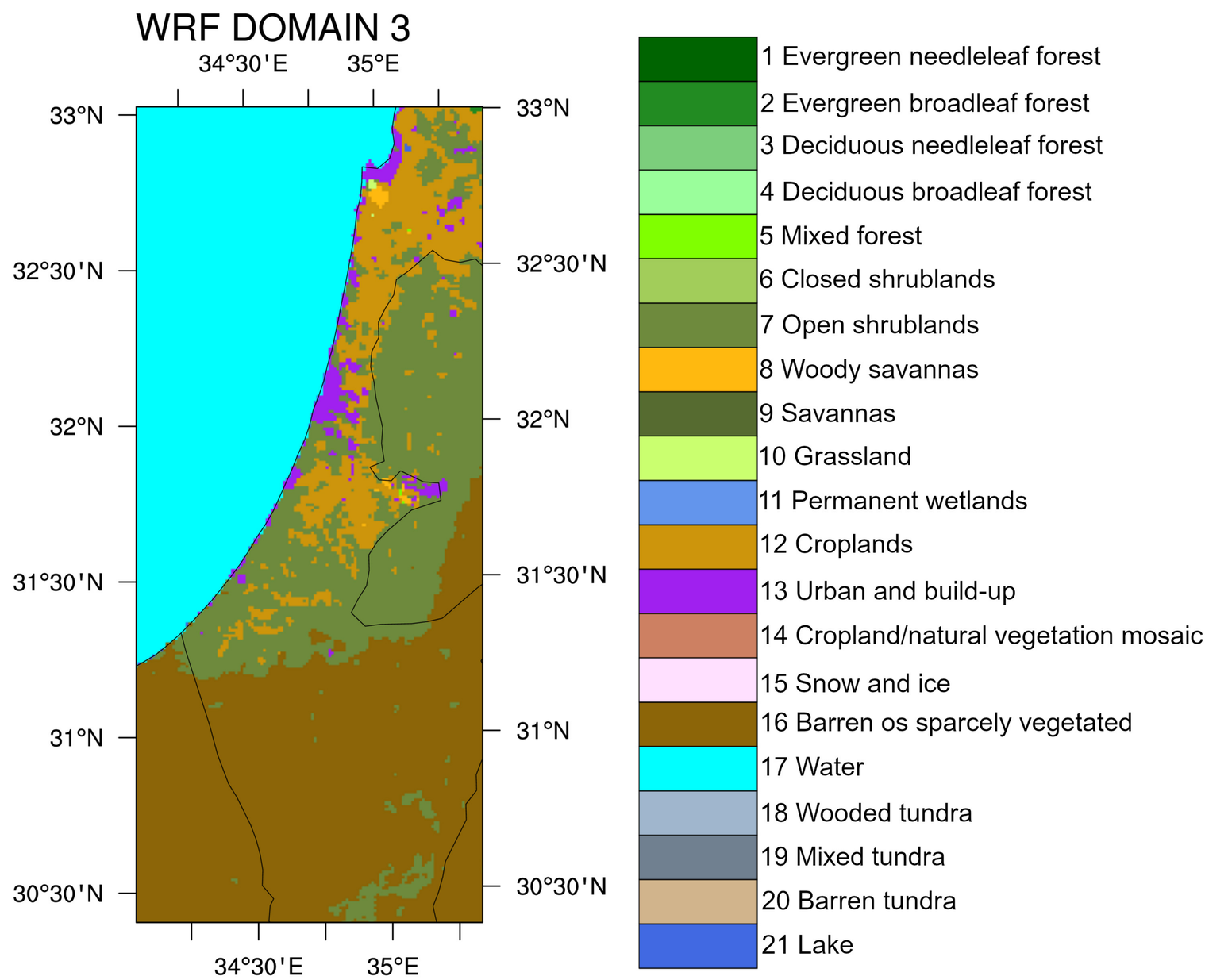
WRF DOMAIN 3
34°30'E
35°E
33°N
32°30'N
32°N
31°30'N
31°N
30°30'N
1 Evergreen needleleaf forest
2 Evergreen broadleaf forest
3 Deciduous needleleaf forest
4 Deciduous broadleaf forest
5 Mixed forest
6 Closed shrublands
7 Open shrublands
8 Woody savannas
9 Savannas
10 Grassland
11 Permanent wetlands
12 Croplands
13 Urban and build-up
14 Cropland/natural vegetation mosaic
15 Snow and ice
16 Barren os sparcely vegetated
17 Water
18 Wooded tundra
19 Mixed tundra
20 Barren tundra
21 Lake

Figure 3.

(a) Jan 3, 2021, 00 UTC

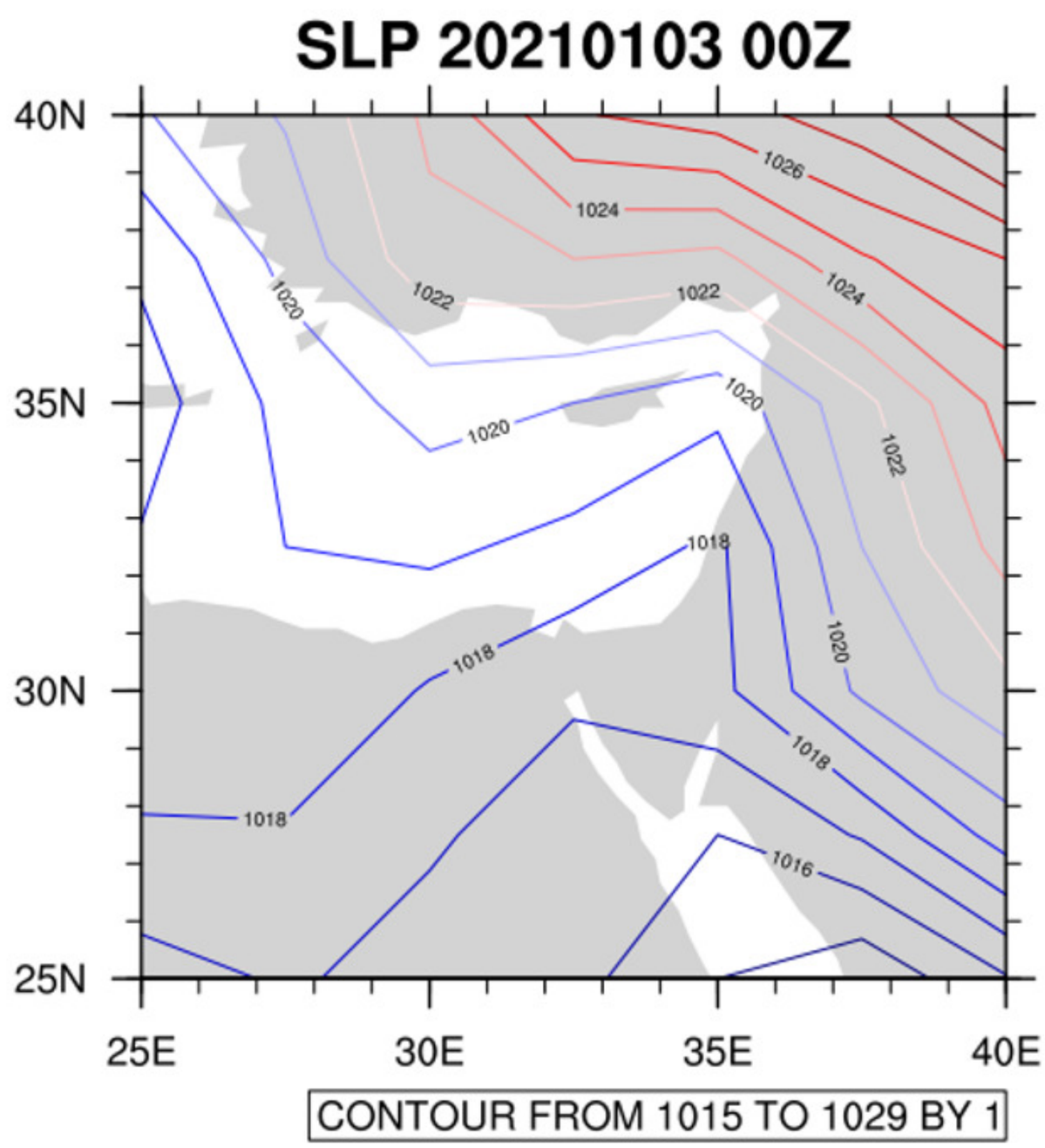

(b) Jan 4, 2021, 00 UTC

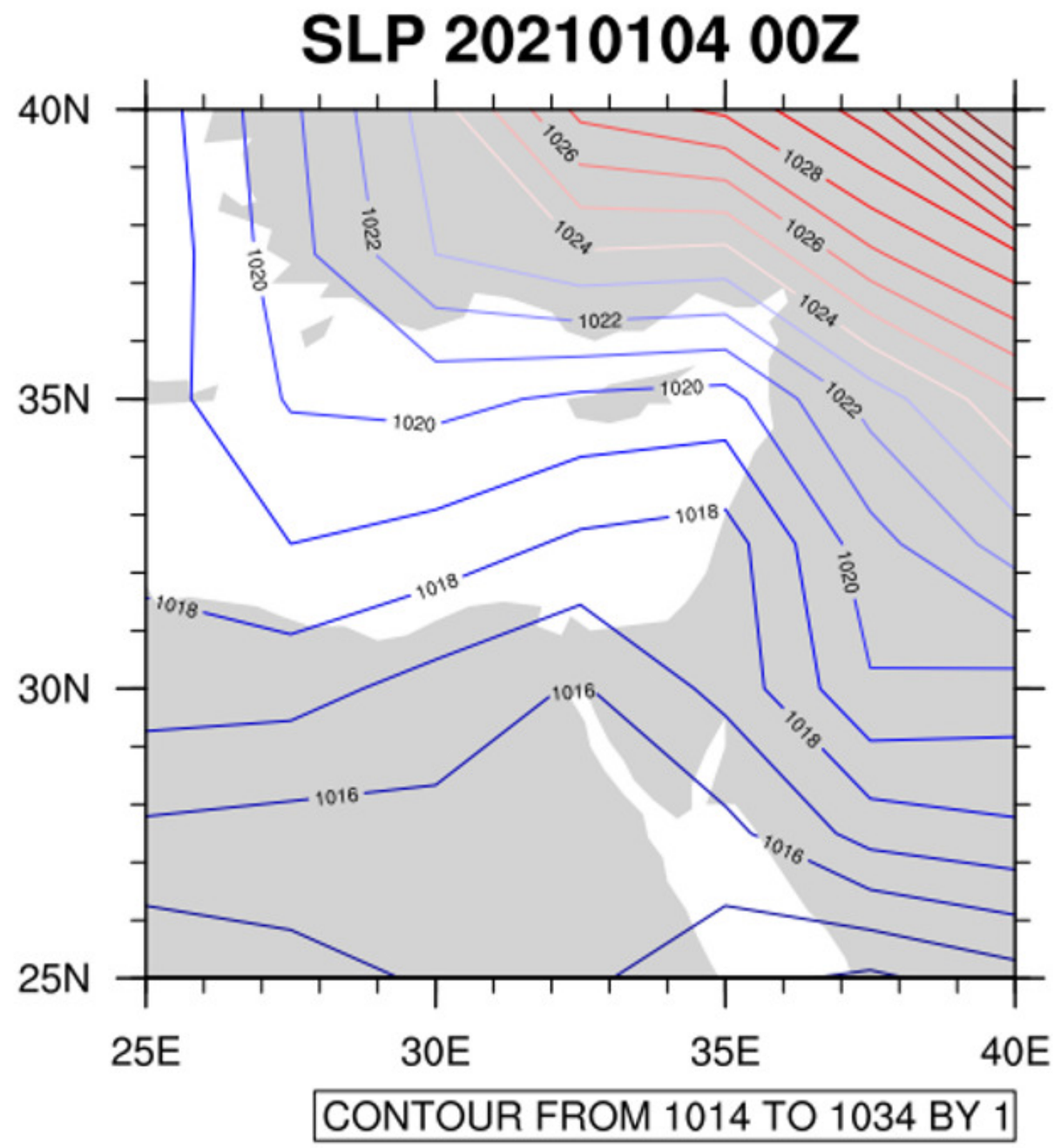

(c) Jan 5, 2021, 00 UTC

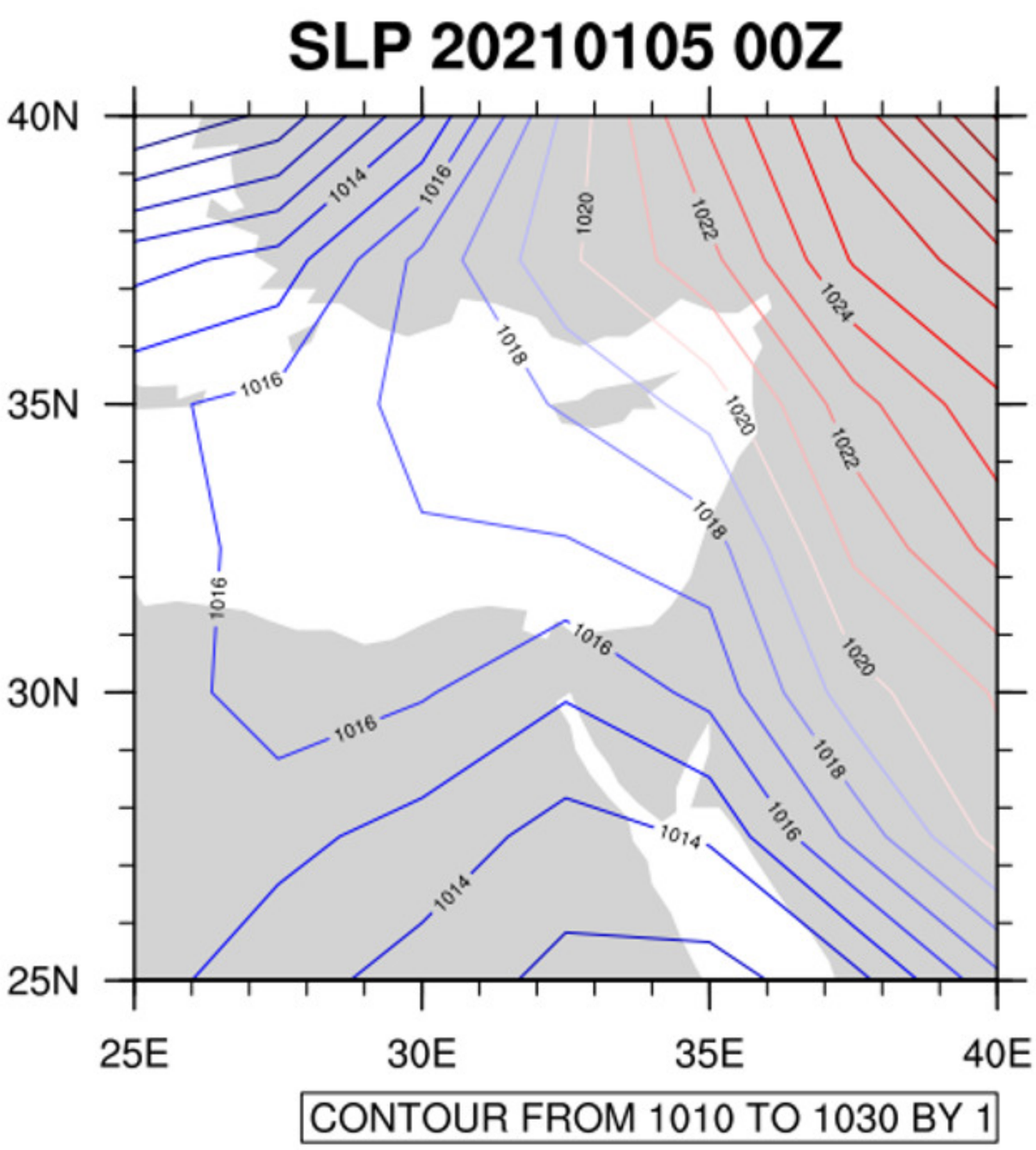

(d) Jan 6, 2021, 00 UTC

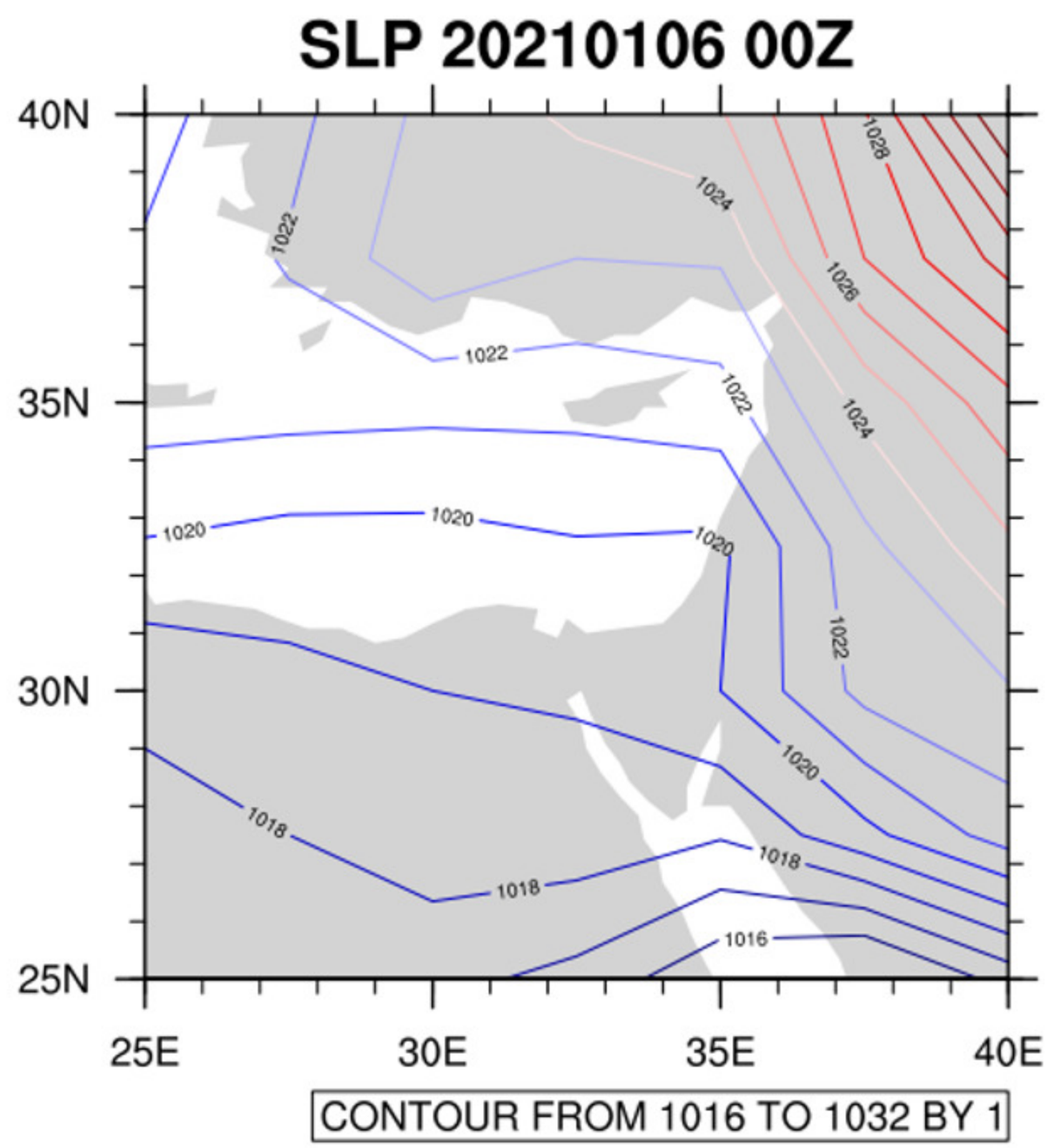

Figure 4.

(a) Jan 3, 2021, 00 UTC

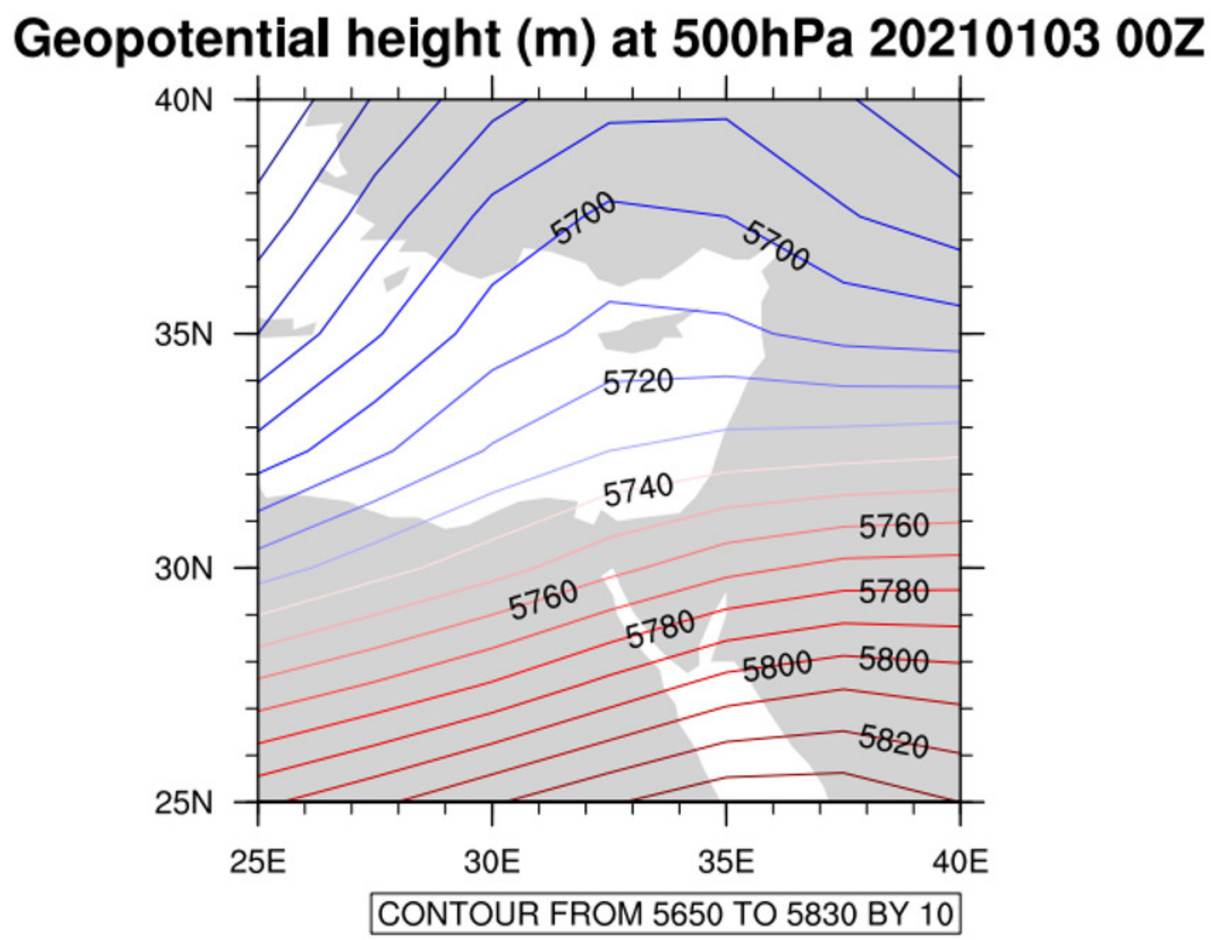

(b) Jan 4, 2021, 00 UTC

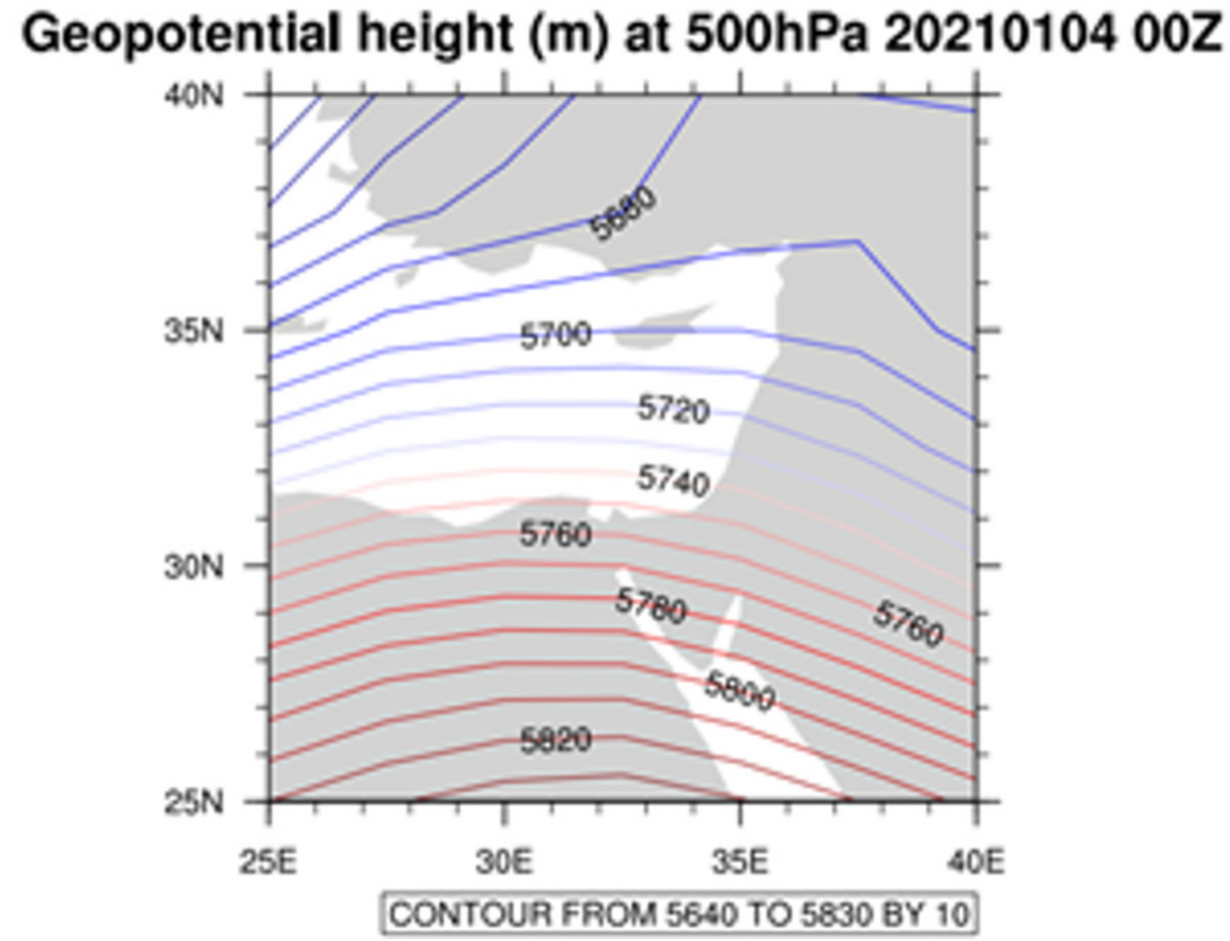

(c) Jan 5, 2021, 00 UTC

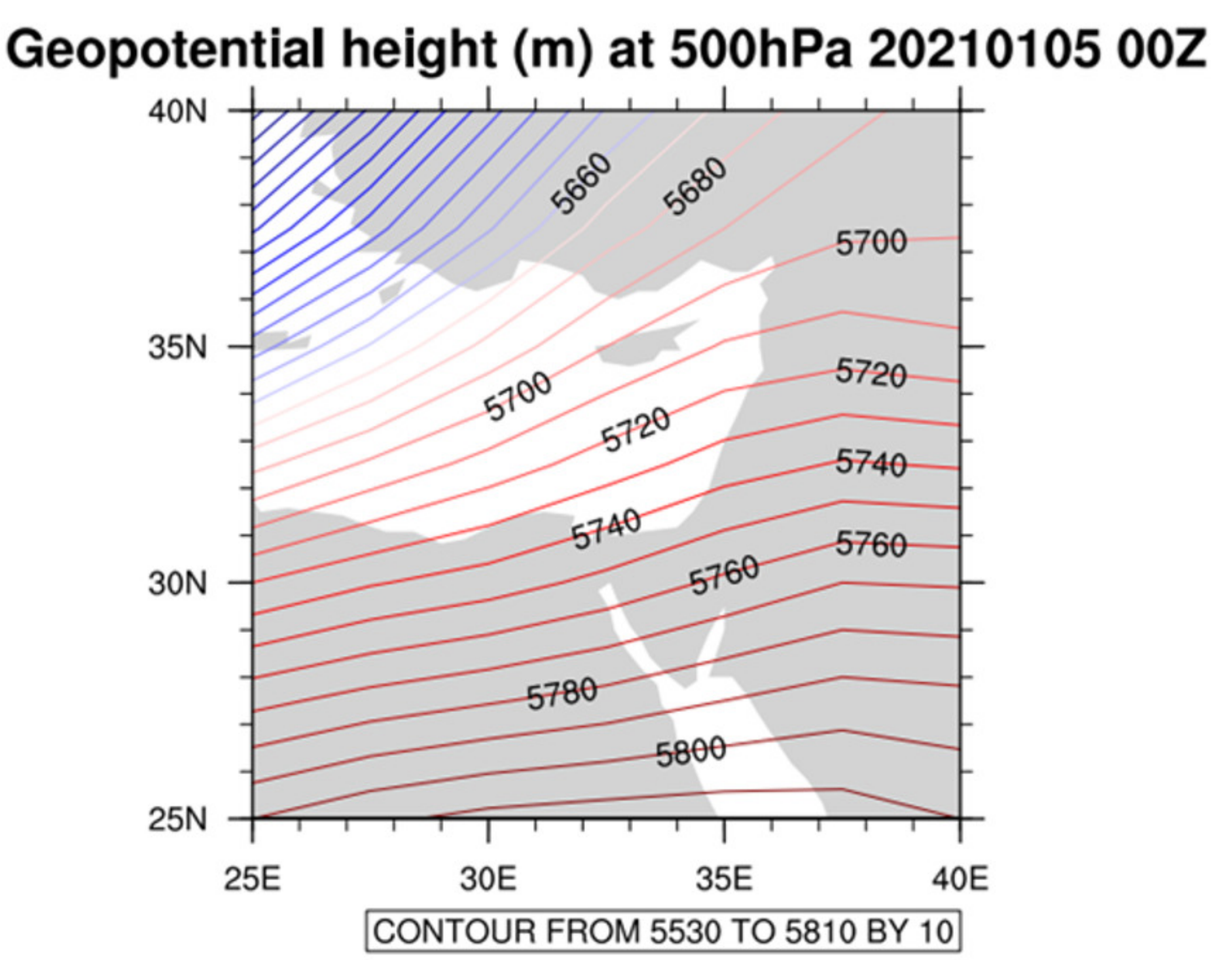

(d) Jan 6, 2021, 00 UTC

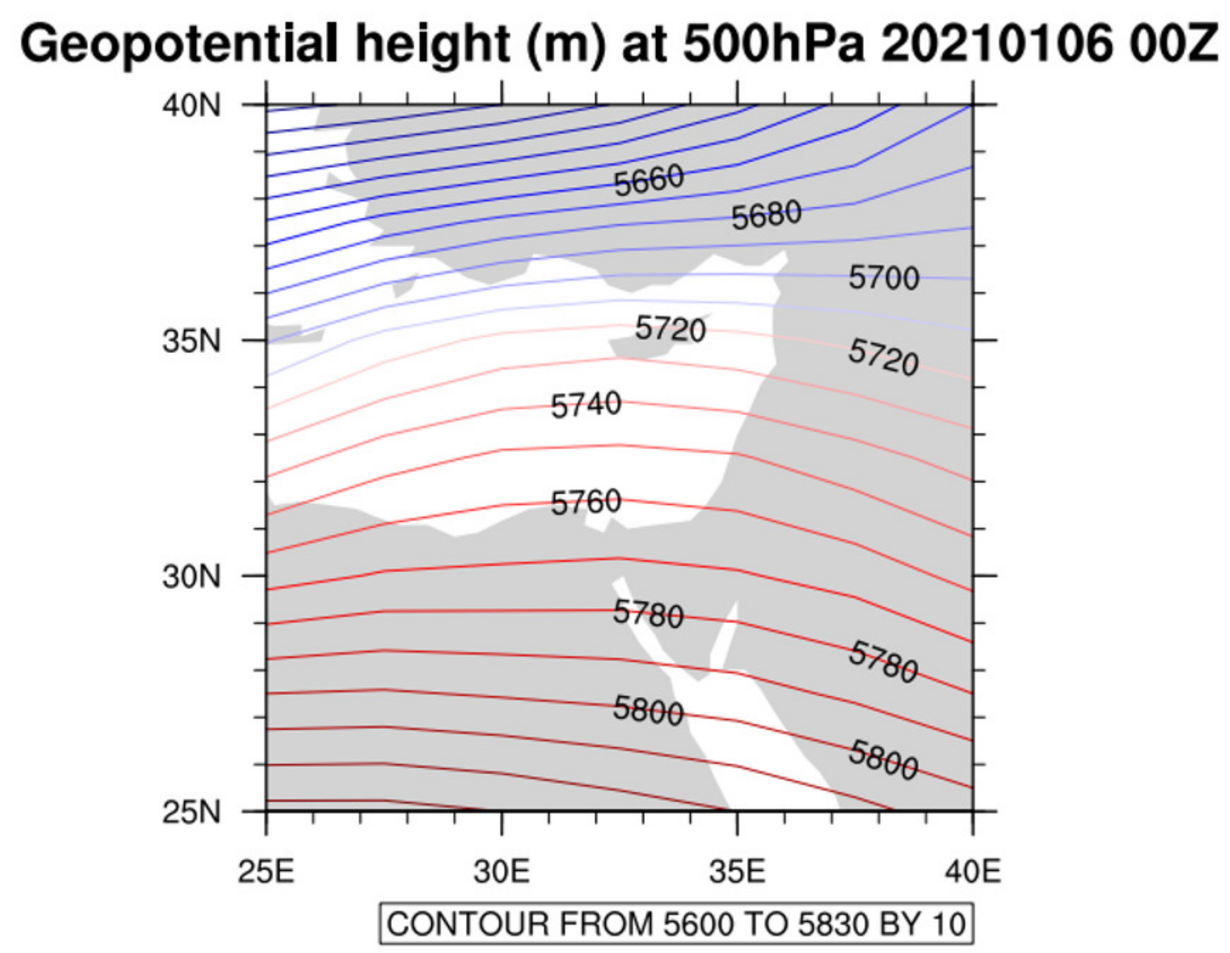

Figure 5.

(a) Jan 3, 2021, 00 UTC

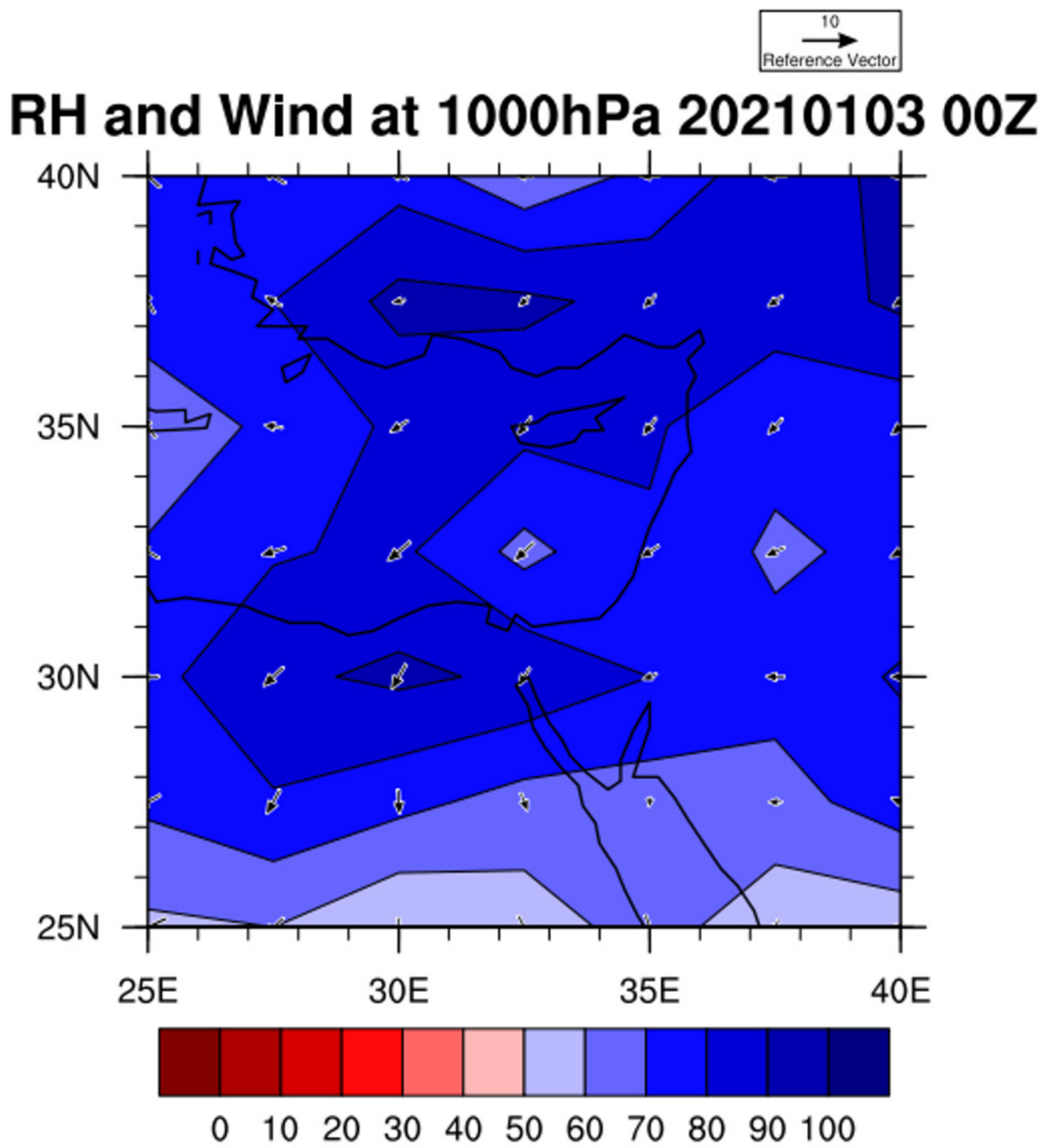

(b) Jan 4, 2021, 00 UTC

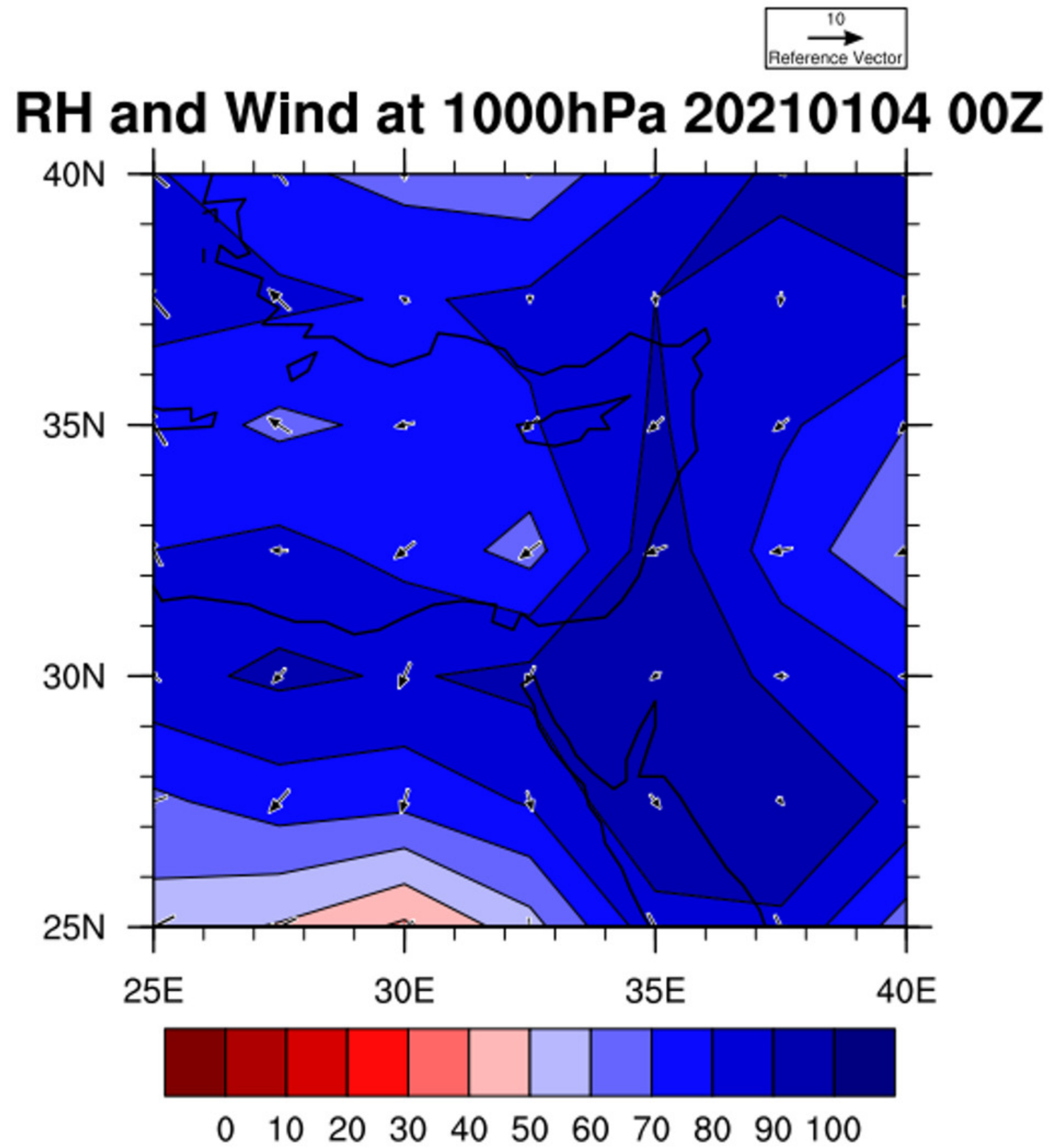

(c) Jan 5, 2021, 00 UTC

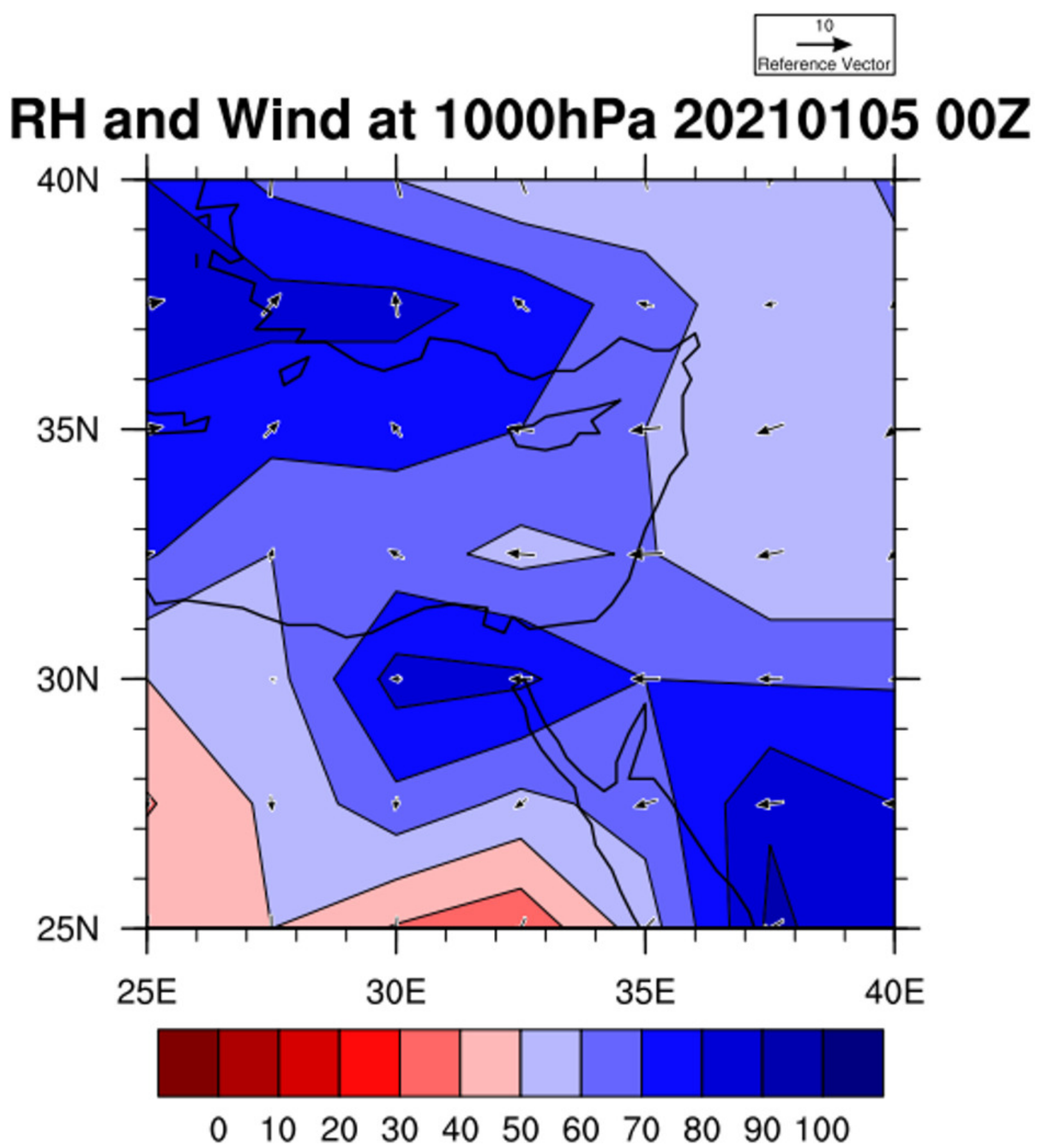

(d) Jan 6, 2021, 00 UTC

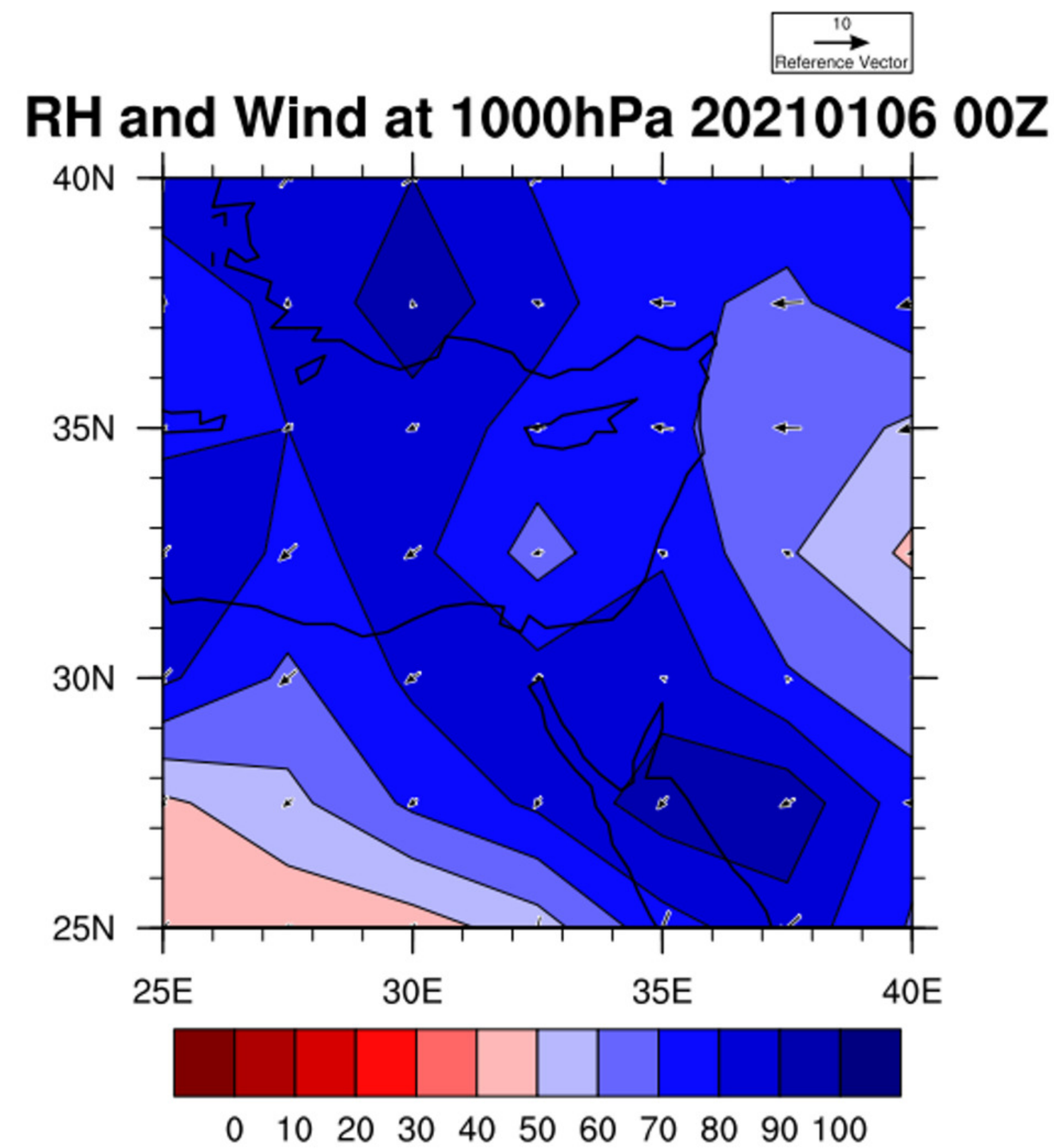

Figure 6.

(a) Jan 3, 2021, 00 UTC

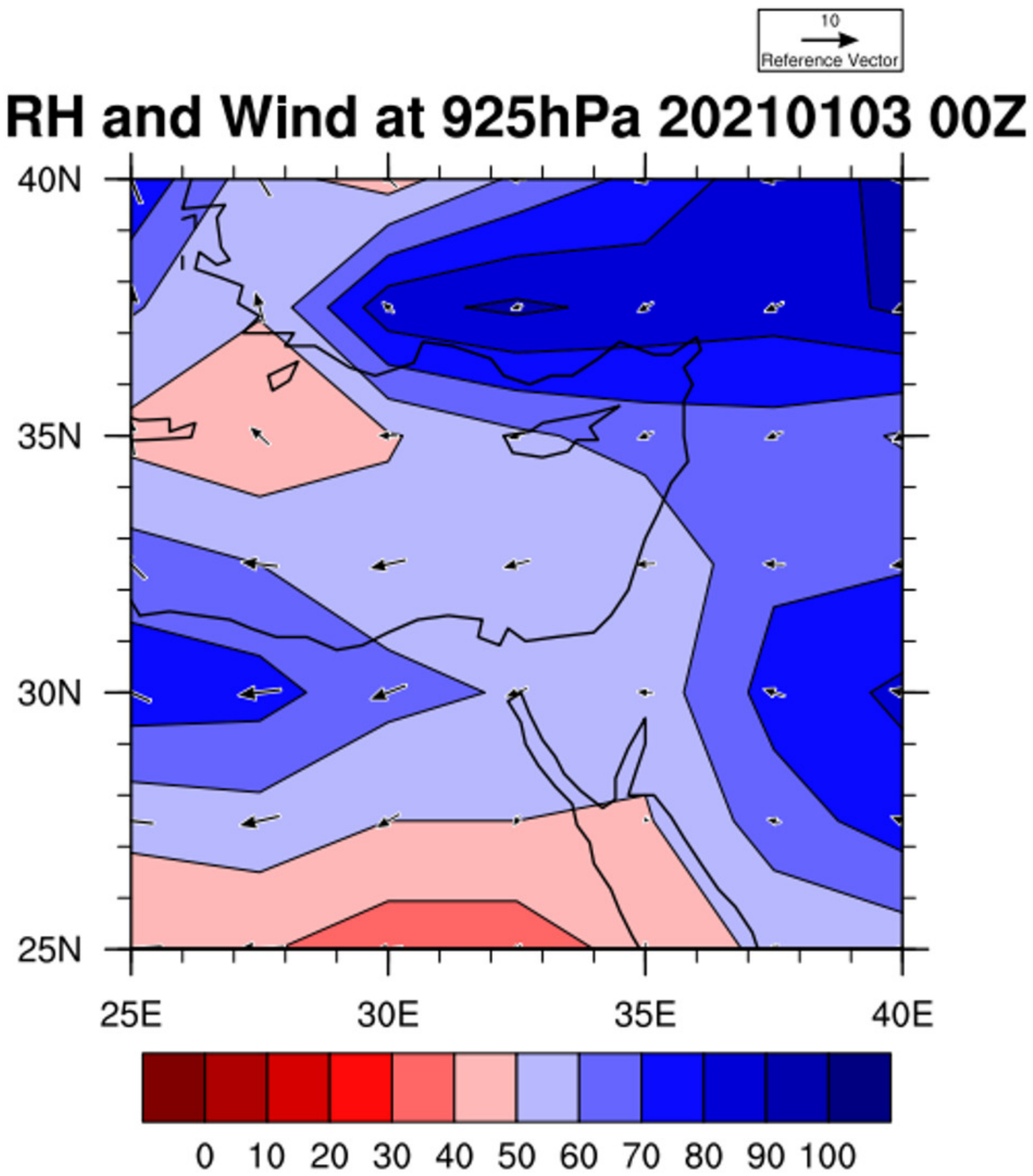

(b) Jan 4, 2021, 00 UTC

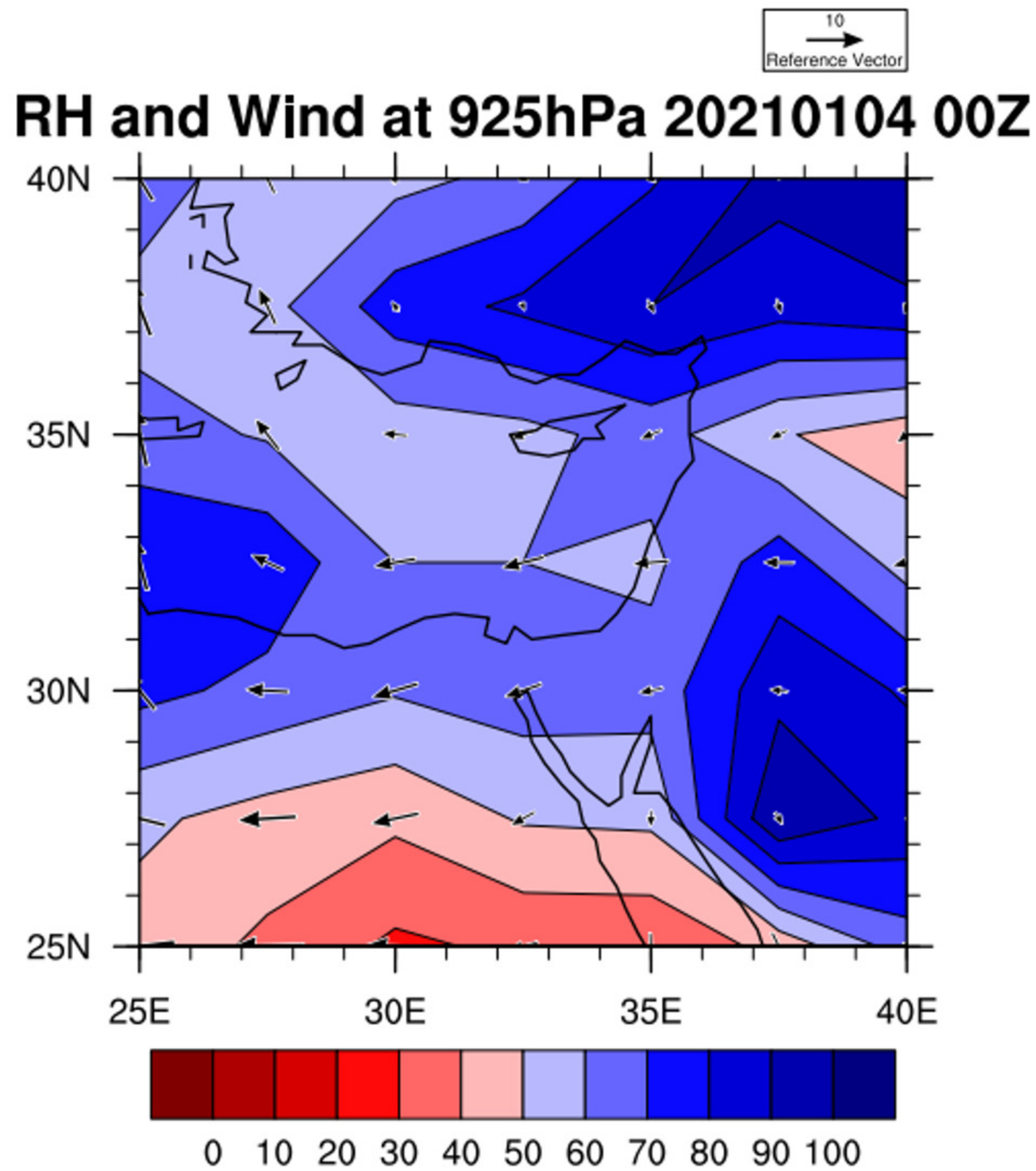

(c) Jan 5, 2021, 00 UTC

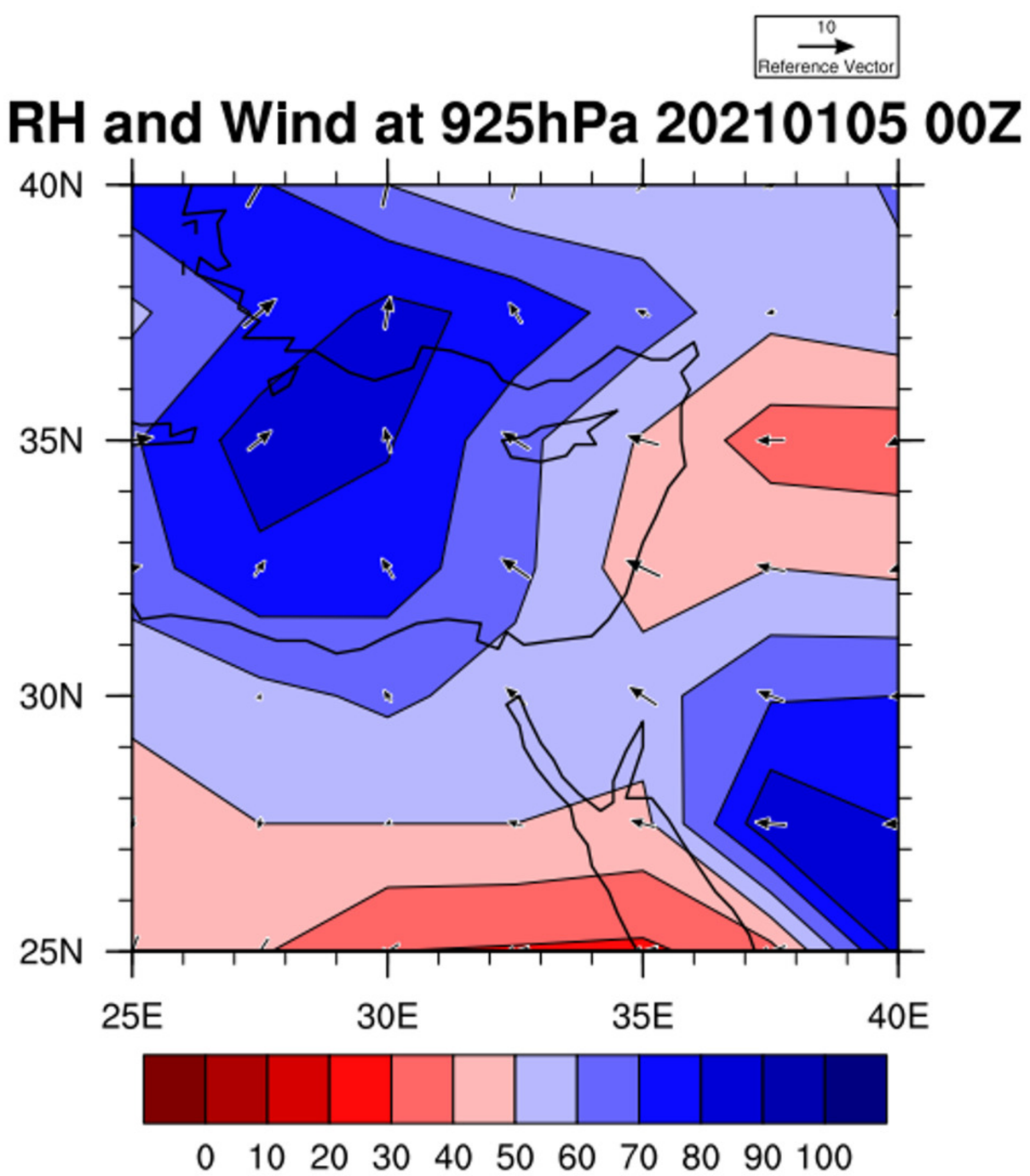

(d) Jan 6, 2021, 00 UTC

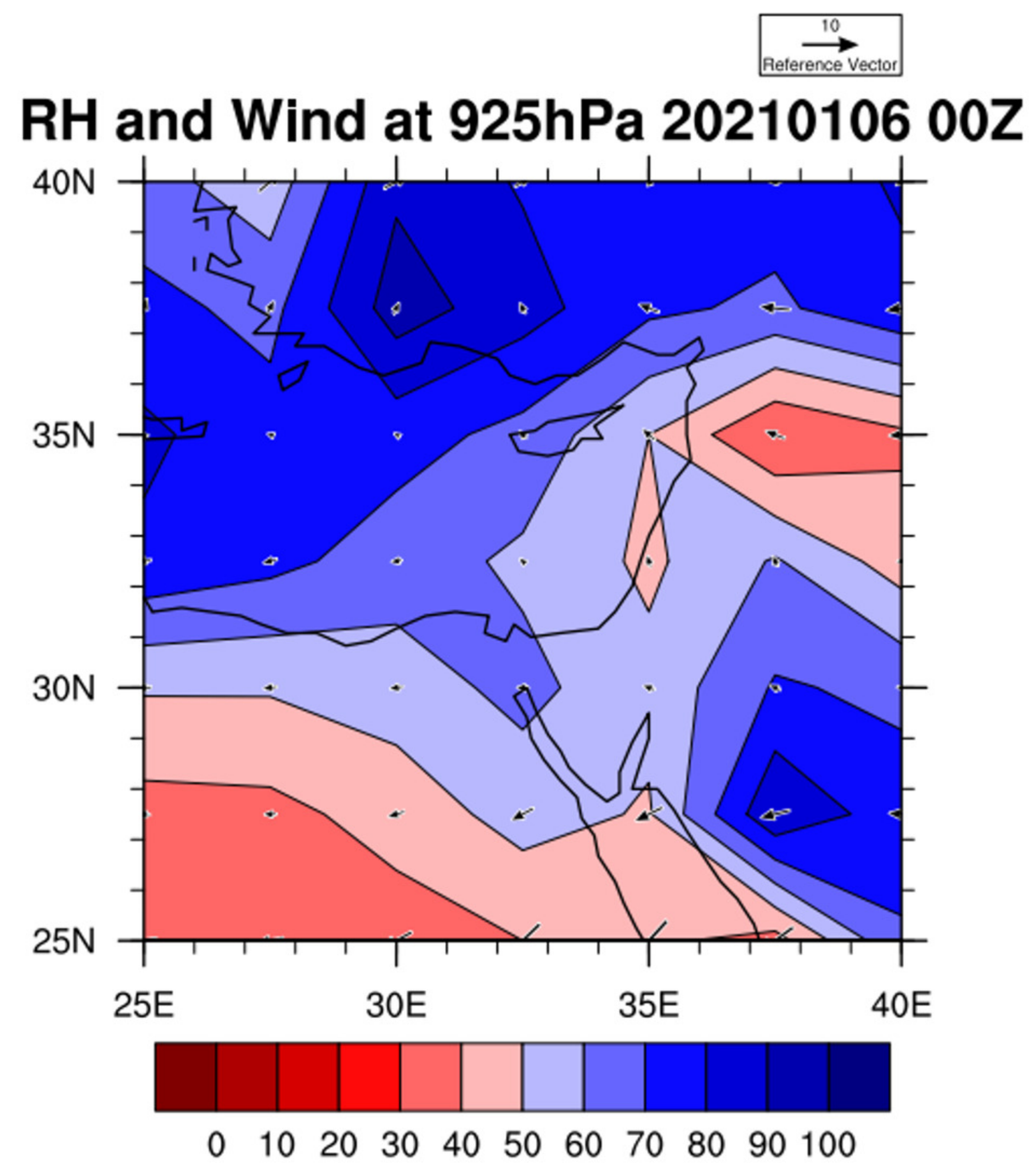

Figure 7.

2021-01-06 00:00

Ground level

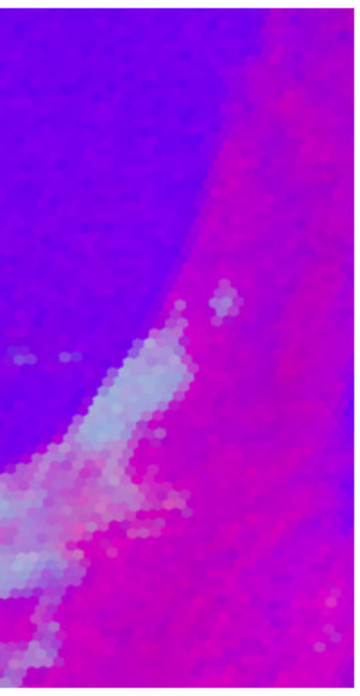

975 hPa level

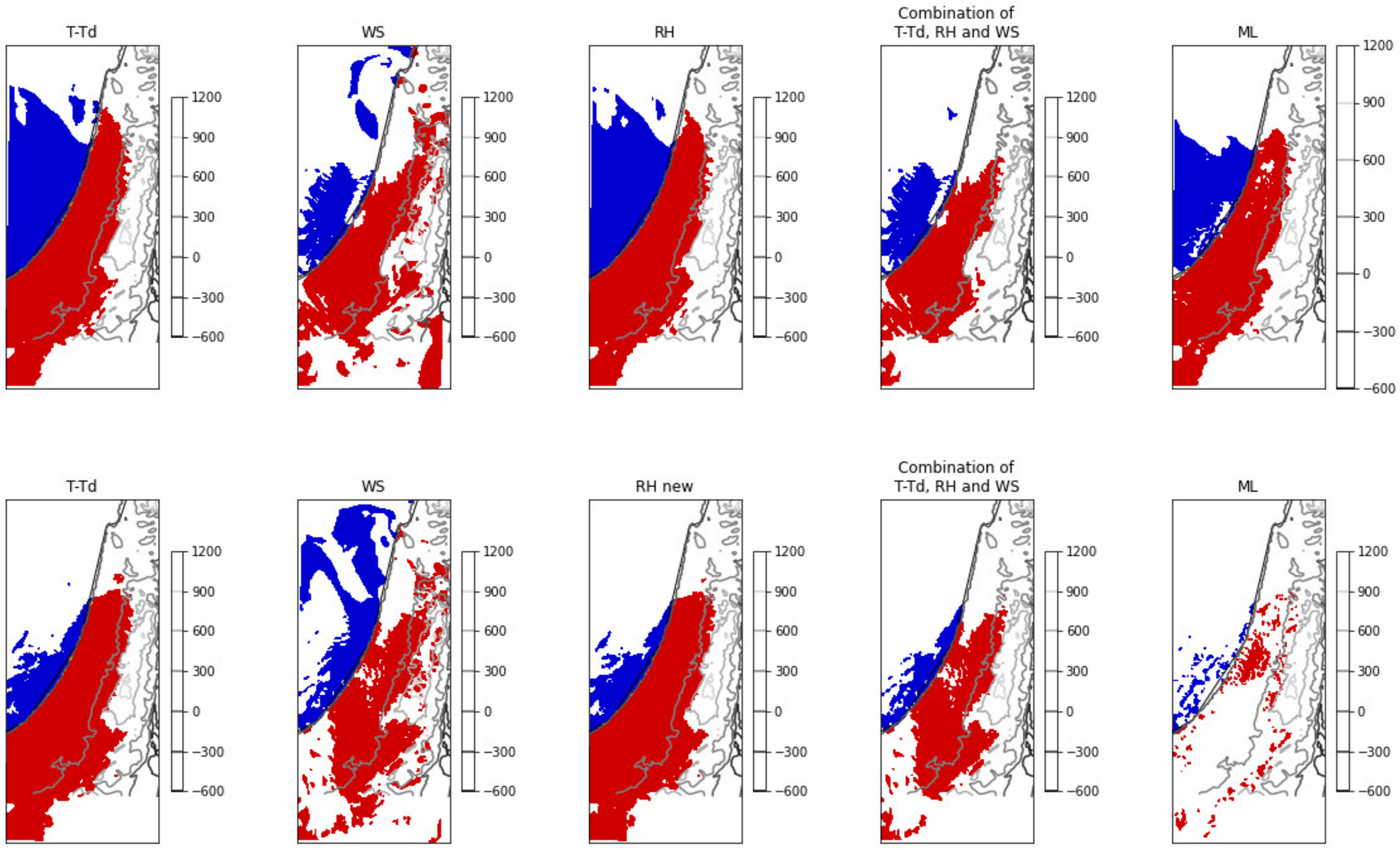

2021-01-06 02:00

Ground level

975 hPa level

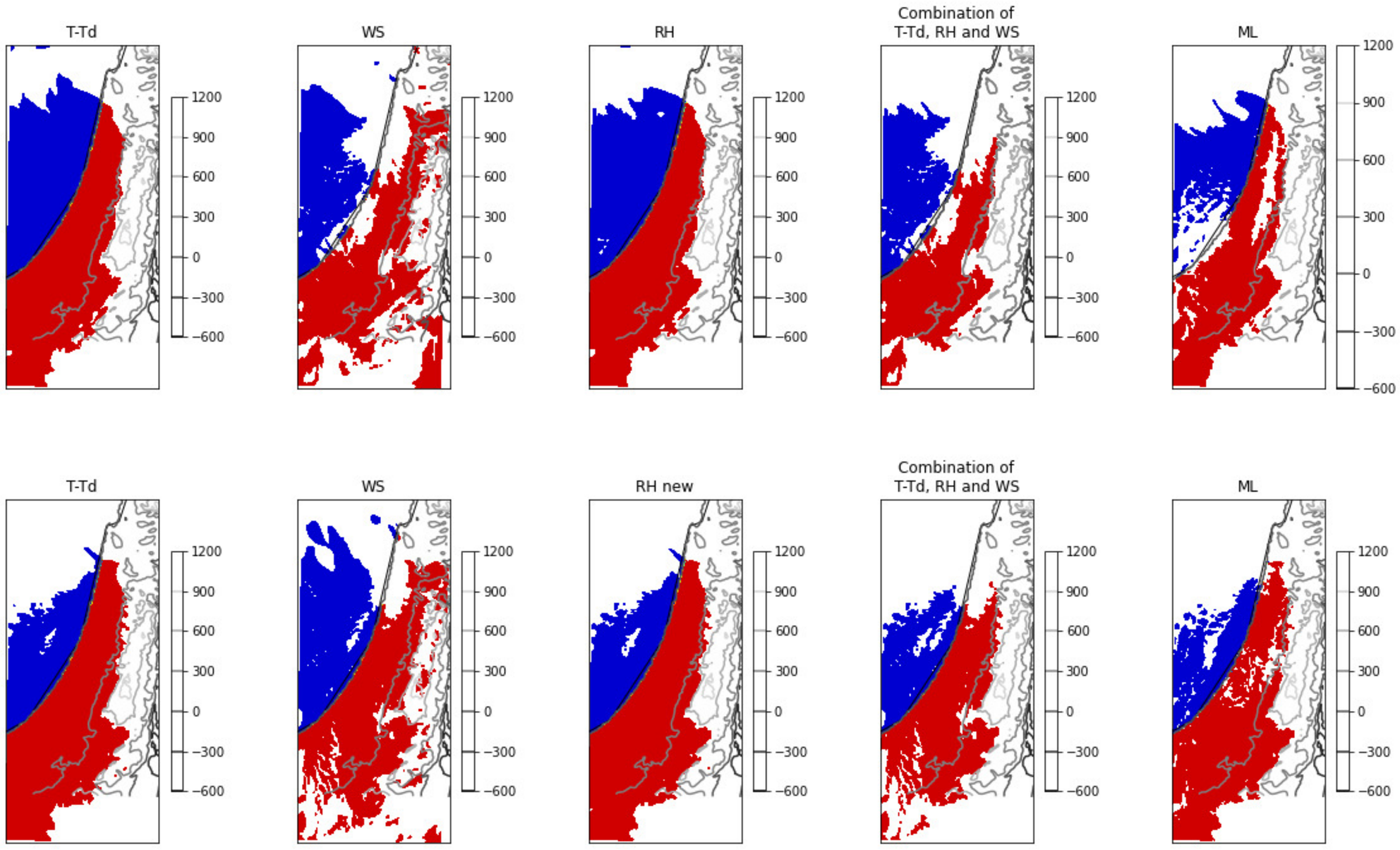

2021-01-06 04:00

Ground level

975 hPa level

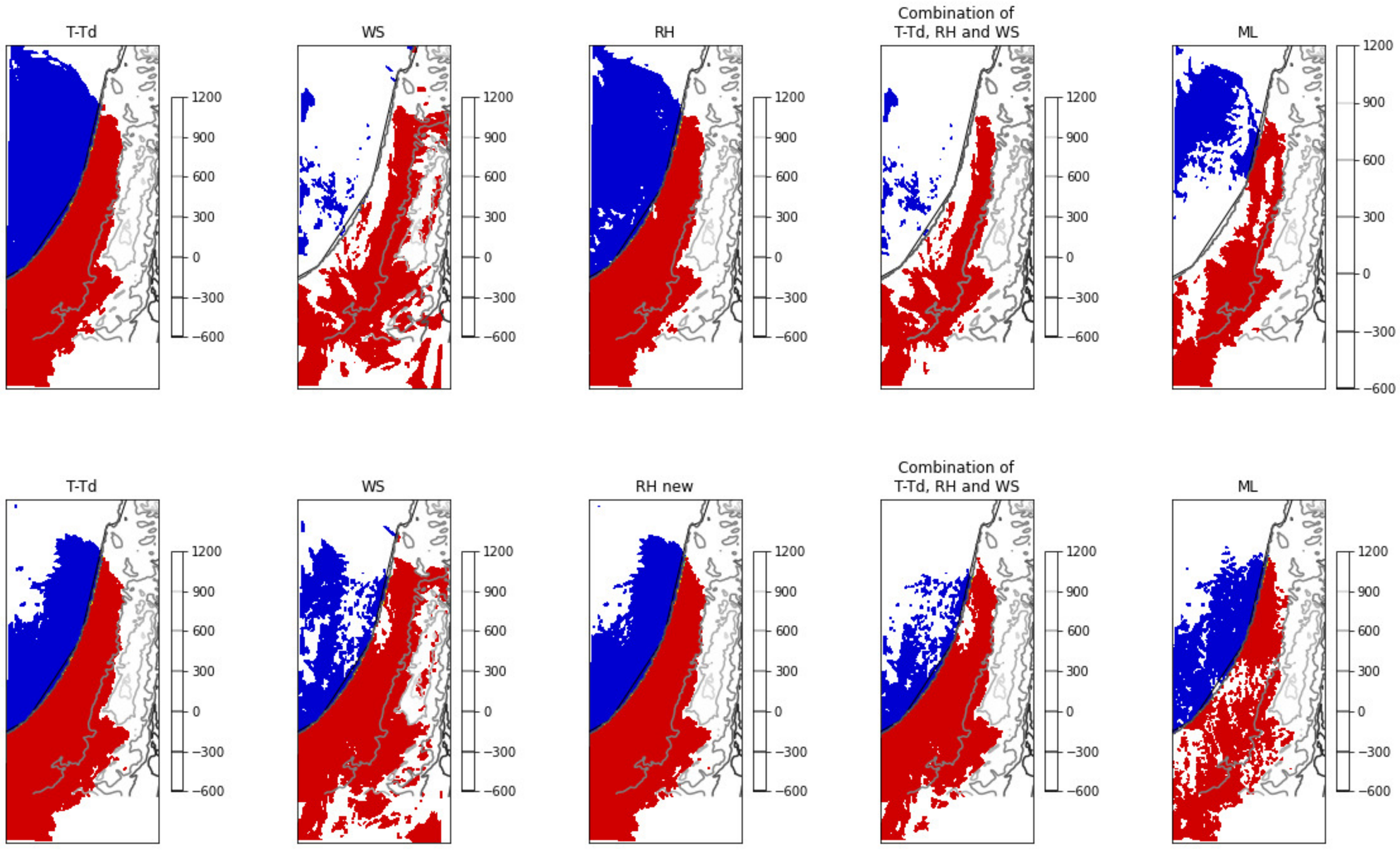

Figure 8.

2021-01-06 06:00:00

Ground level

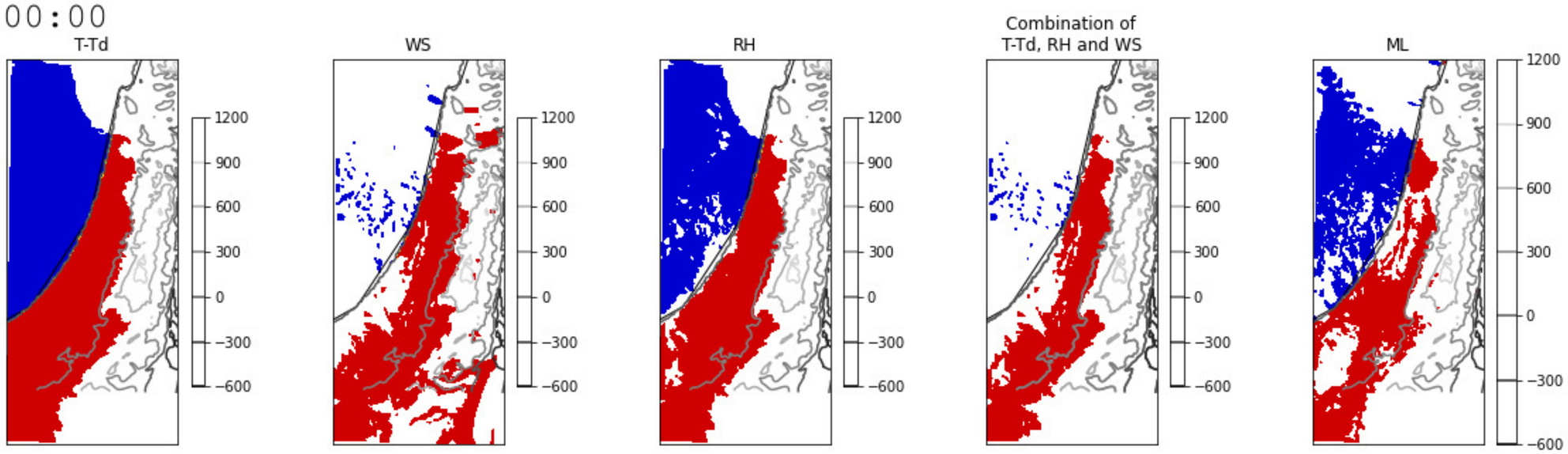

975 hPa level

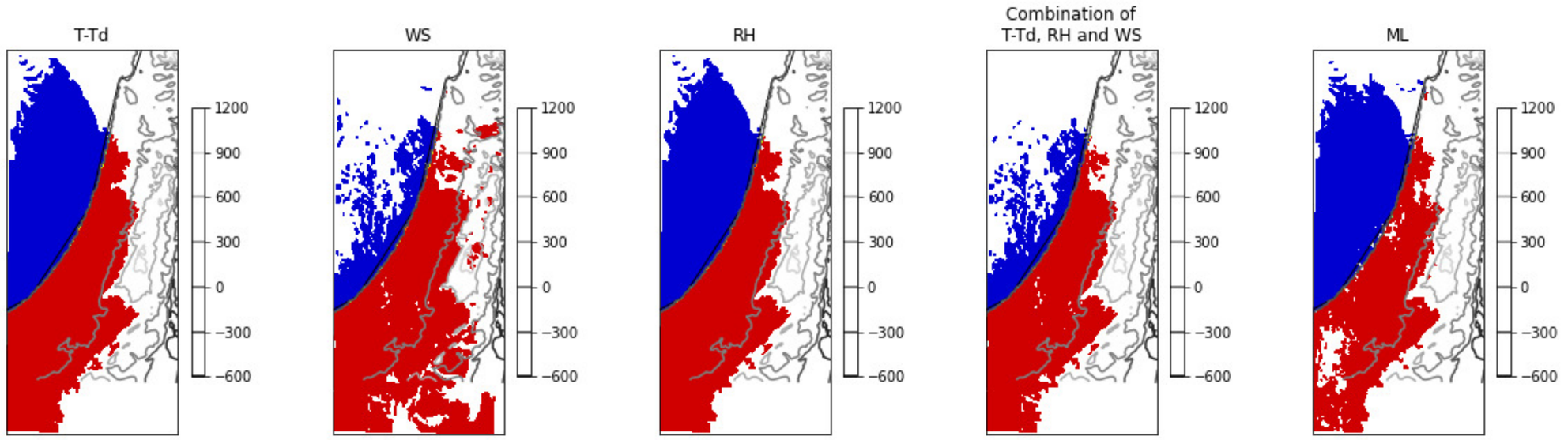

2021-01-06 08:00:00

Ground level

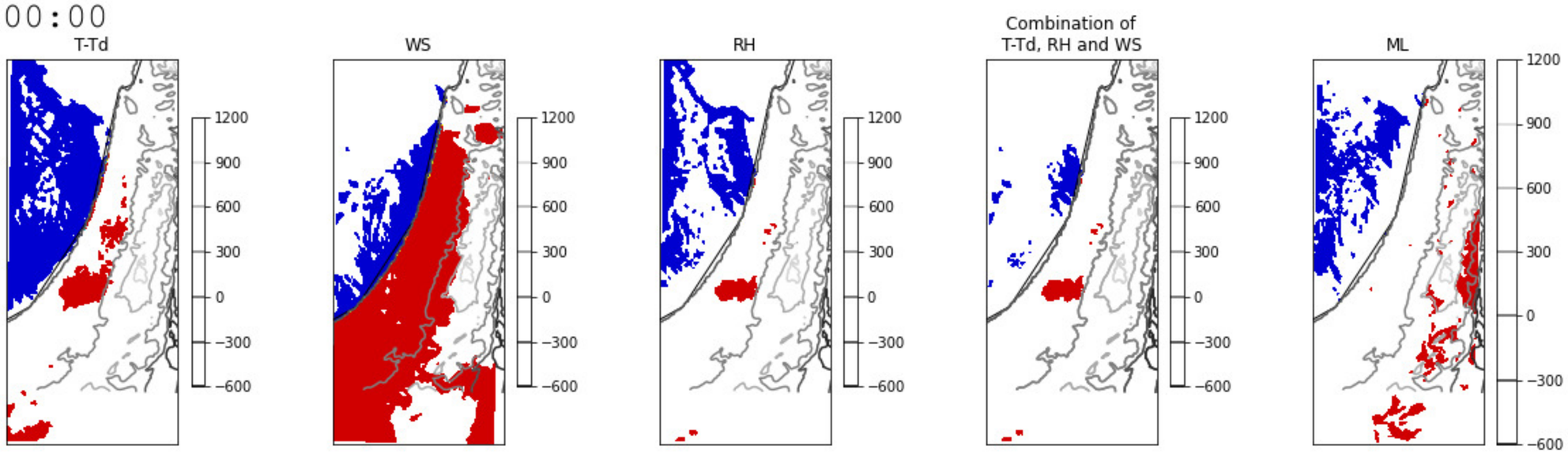

975 hPa level

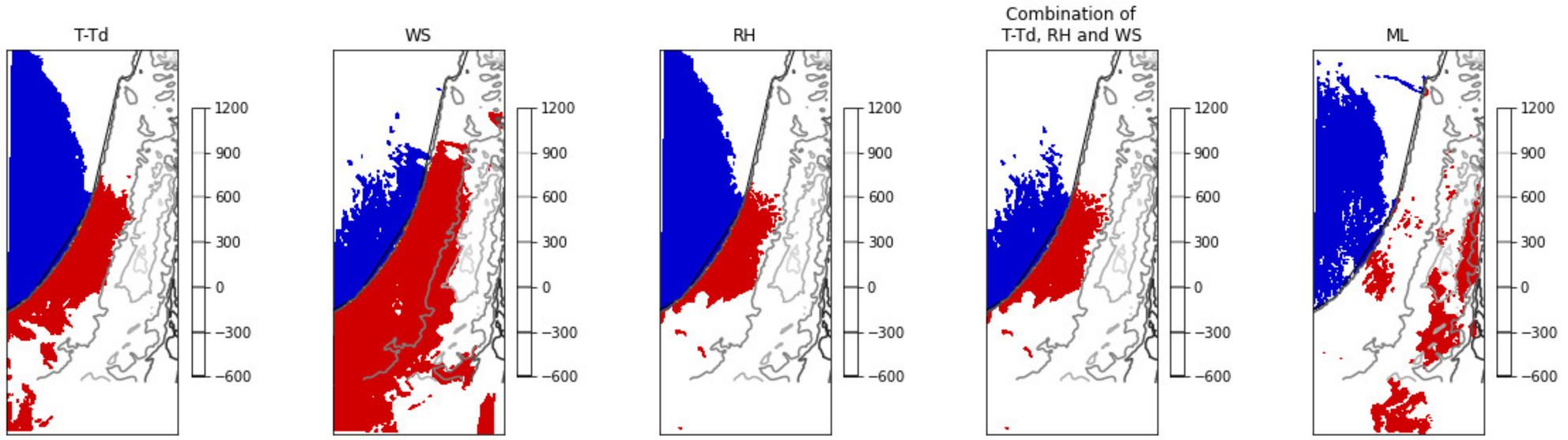

Figure 9.

Radiosonde : Beit dagan vs WRF , 05/01/21 23 UTC

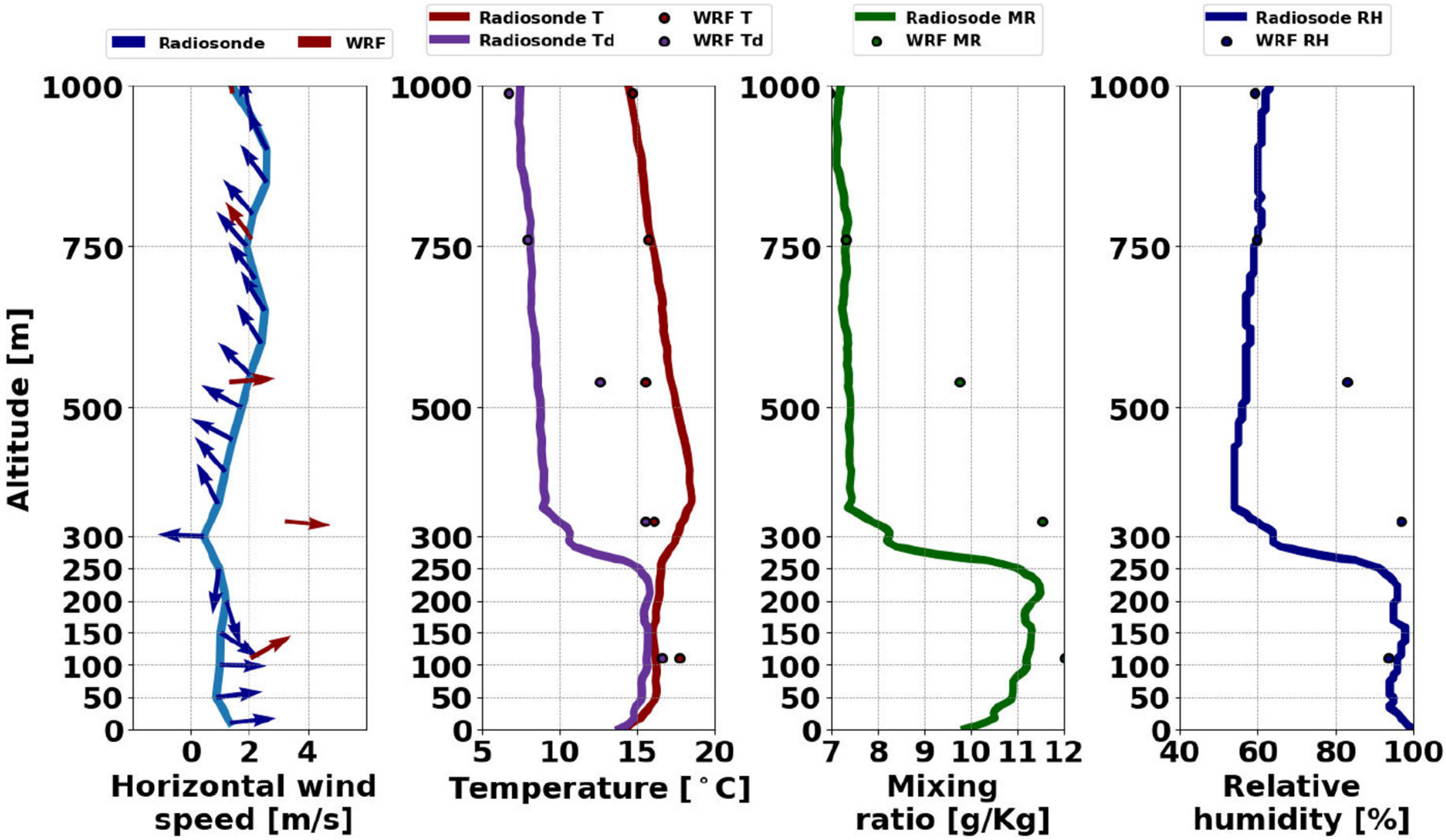

Figure 10.

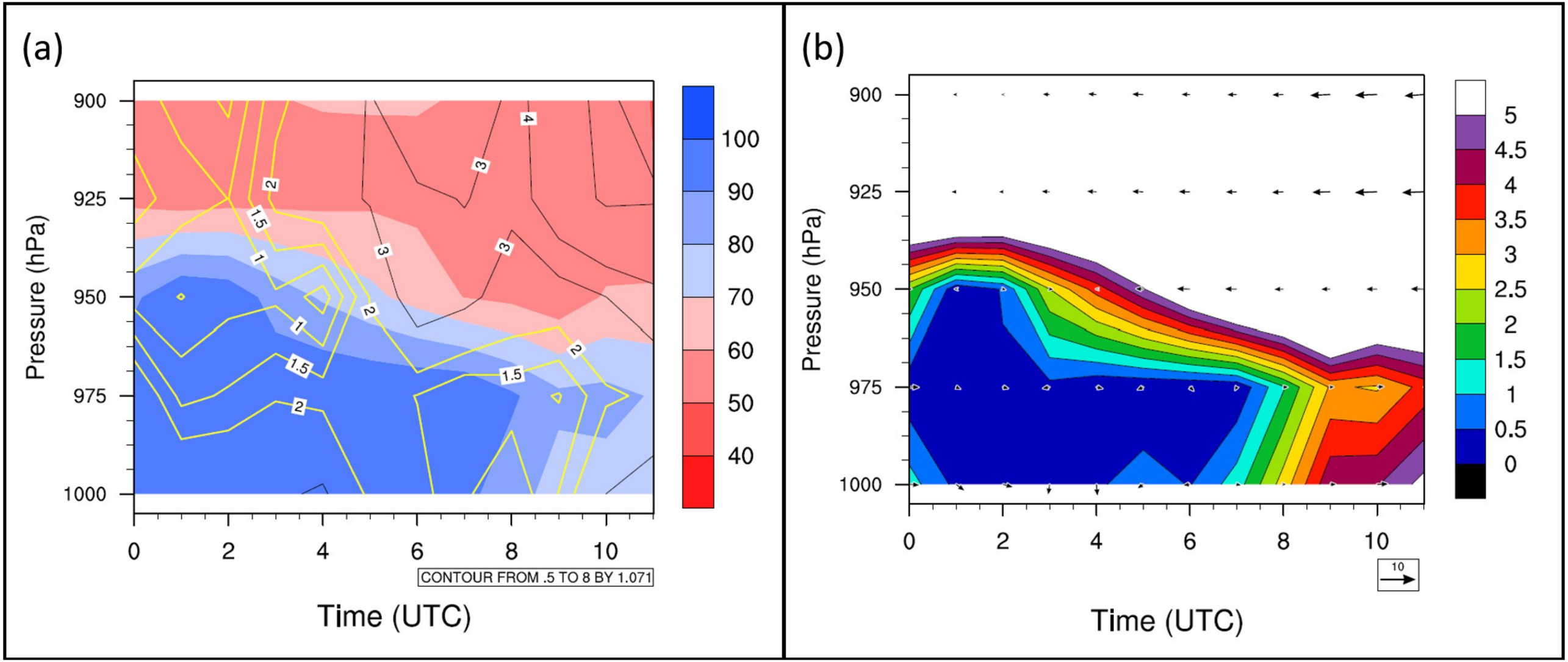
(a)
Pressure (hPa)
900
925
950
975
1000
0
2
4
6
8
10
Time (UTC)
CONTOUR FROM .5 TO 8 BY 1.071
100
90
80
70
60
50
40
(b)
Pressure (hPa)
900
925
950
975
1000
0
2
4
6
8
10
Time (UTC)
10
5
4.5
4
3.5
3
2.5
2
1.5
1
0.5
0

Figure 11.

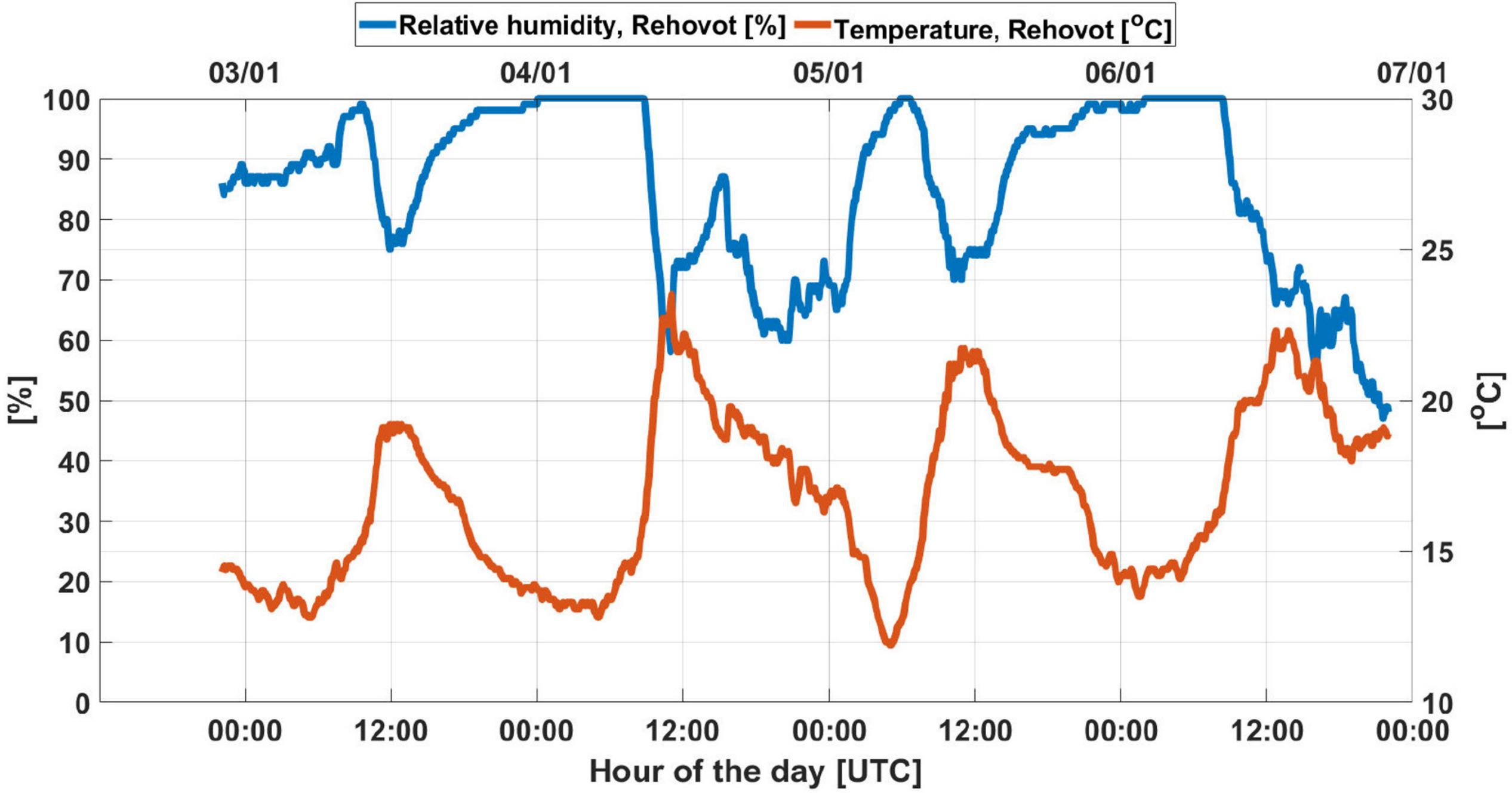
Relative humidity, Rehovot [%]
Temperature, Rehovot [°C]
03/01
04/01
05/01
06/01
07/01
100
90
80
70
60
50
40
30
20
10
0
[%]
30
25
20
15
10
[°C]
00:00
12:00
00:00
12:00
00:00
12:00
00:00
12:00
00:00
Hour of the day [UTC]

Figure 12.

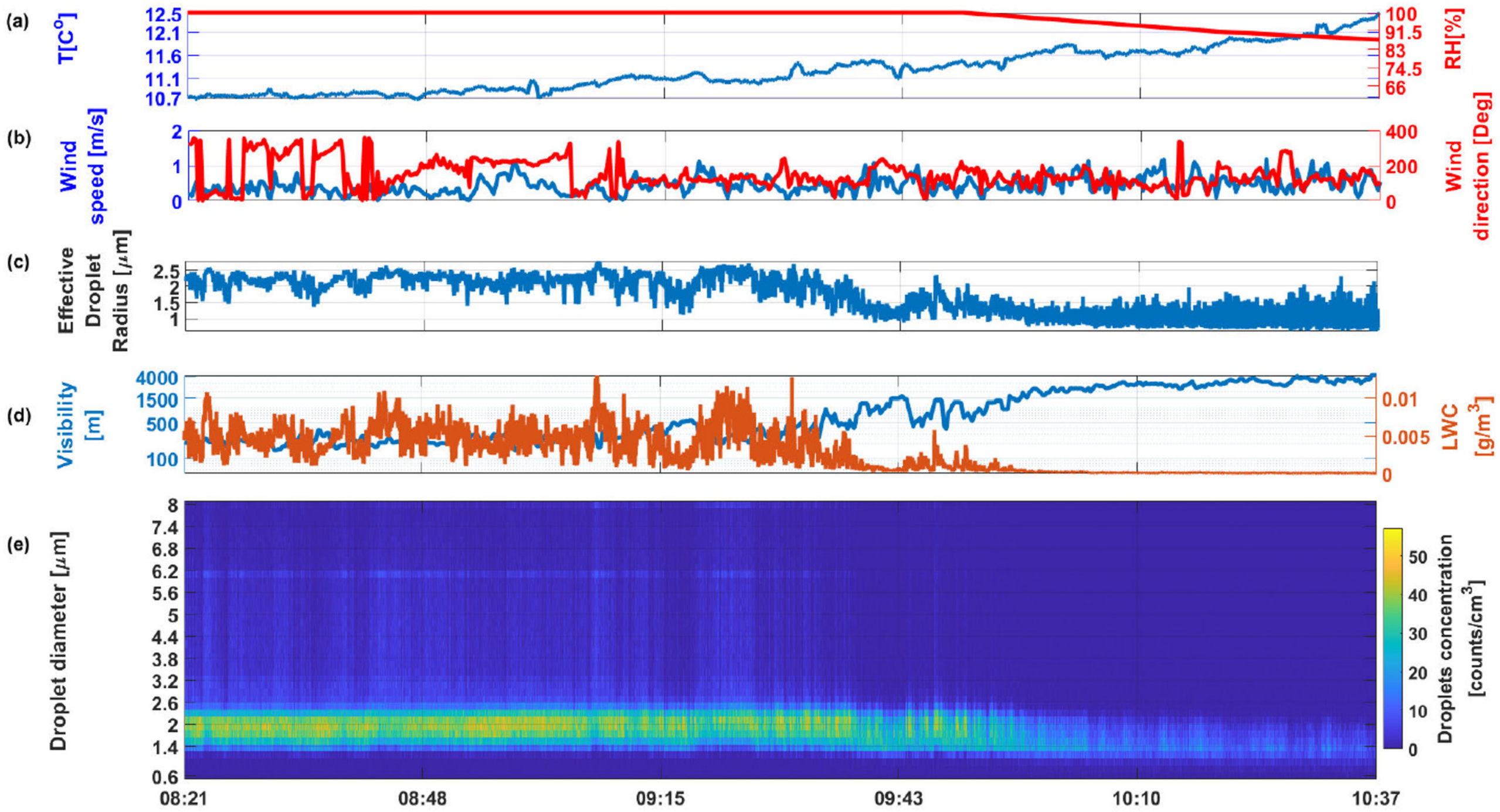
(a)
T[C°]
12.5
12.1
11.6
11.1
10.7
RH[%]
100
91.5
83
74.5
66
(b)
Wind speed [m/s]
2
1
0
Wind direction [Deg]
400
200
0
(c)
Effective Droplet Radius [μm]
2.5
2
1.5
1
(d)
Visibility [m]
4000
1500
500
100
LWC [g/m3]
0.01
0.005
0
(e)
Droplet diameter [μm]
8
7.4
6.8
6.2
5.6
5
4.4
3.8
3.2
2.6
2
1.4
0.6
Droplets concentration [counts/cm3]
50
40
30
20
10
0
08:21
08:48
09:15
09:43
10:10
10:37